Quantum Dynamics of Hydrogen on Ruthenium

Jolyon Aarons

Submitted for the Degree of
MSc by Research

Department of Physics
University of York

May 2013

Abstract

A study of Hydrogen dynamics on a simple model Ruthenium surface has been performed using Partially Adiabatic Centroid Molecular Dynamics (PACMD), with a stochastic, Langevin based thermostat. Evidence has been found, and is presented within for quantum-mechanically mediated, temperature-dependent friction. The technique has been shown to accurately model the dynamics, as measured experimentally by Helium-3 Spin-echo Interferometry, in a way which has not been possible with classical techniques.

Contents

List of Figures

List of Tables

List of Algorithms

Declarations

I declare that the work presented in this thesis, except where otherwise stated, is based on my own research and has not been submitted previously for a degree in this or any other university. Parts of the work reported in this thesis have been published in:

Signed

Jolyon Aarons

Acknowledgements

I would like to thank Dr. Matt Probert for his time and wisdom and Dr. Phil Hasnip for a seemingly unending stream of ideas. Dr. Eliza McIntosh in Cambridge has served to push the project forward whenever I have flagged; provided a great deal of insight and time, together with many resources which have helped me at every turn. I would also like to thank Dr. Bill Allison of Cambridge who has been incredibly patient with me and helped me feel at home whenever I have visited the Cavendish. I have asked a great many questions of Michele Ceriotti about the GLE method, who has been gracious throughout and answered even the most trivial of them helpfully. I would like to thank Professor David Manolopoulos for a very useful discussion on generating ISFs and for having answered my questions by email. Dr. Dave Ward of Cambridge also went out of his way to cycle out and by a hard disk when we ran out of disk space, so many thanks. I would also like to thank the Rex Godby, Chris Fewster and Joerg Meyer for very useful discussions. Finally, thanks to everyone in N102 for an enjoyable year and to Jingdi for always being there.

This thesis is dedicated to my family.

Chapter 1

Introduction

As long as physics has been recognisable as the discipline it has become, simplification has been the key to understanding. From the early shell models of atomic electron configuration, to the free electron (Drude-Sommerfeld) model of metallic valence electron behaviour, to the local density approximation for the exchange-correlation energy in density functional theory, models may not explain everything about a system, but as long as they serve to describe at least part of the phenomenology a great deal may be elucidated.

Modelling and theory are only half of the picture, however, as experiment serves to both provide the inspiration for and to prove or disprove the efficacy of an upgraded model. Of course, a model can also be used to predict, and so to inspire the design of subsequent experiments to gather new evidence in support of a claim.

Surfaces, the interface between a solid and another phase, have been some of the most studied systems in condensed matter physics. While a surface could be thought of as a simplified analogue for the bulk, this would be entirely wrong. Many effects seen on surfaces are not present at all in the bulk and have served to show that not only can surfaces be very complicated systems, but so much so that an entire field; surface science grew to address the unusual behaviour encountered on them.

Surface effects are of huge importance technologically, for instance in catalysis, the catalyst is often a solid, with gas or liquid phase reactants. An important factor in the catalysed reaction rate is often the amount of surface area of the catalyst presented to the reactants. In semiconductor microelectronic manufacture, a device is built up on a surface through various processes including sputtering and photolithography which are carefully designed to alter the surface though several steps in order to produce clearly prescribed results when appropriately operated.

This work has been completed as a collaboration between the experimental Cambridge surface science group of Dr. Bill Allison and the group of Dr. Matt Probert in the York university condensed matter theory group.

1.1 Experimental Background

The surface science group in Cambridge has developed the world's first ^3He spin-echo interferometer. A device capable of resolving the dynamics of light adsorbates on surfaces. This builds on both Neutron spin-echo interferometry and ^3He time-of-flight measurements. Neutron scattering is not appropriate for surface experiments as neutrons tend to penetrate into the bulk; ^3He is reflected above the surface atoms, however and hence only samples surface states. The spin-echo technique is important for temporal resolution; time of flight measurements suffer because of the difficulty in precisely controlling the velocity distribution of incident ^3He atoms affects how accurately the measurement of energy transfer from scattered atom to surface can be. The spin-echo technique addresses this by using an imposed spin-moment on the incident atom to effectively time the scattering process internally. The polarisation of the reflected atom encodes this information.

The importance of the experimental kit is, broadly speaking, that it has exceptional spatial and temporal resolution. A property which was necessary, as the equipment has been used to measure the dynamics of hydrogen adsorbed on a ruthenium surface; a fast diffusive process. The measurements of dynamics then lead on to the calculation of diffusion constants which differ depending on the temperature. Classical molecular dynamics simulations were performed by the group, but the results did not align with experimental measurement.

1.2 PIMD Background

Path integral molecular dynamics (PIMD) is a computational technique based upon the path integral formulation of quantum mechanics, first proposed by Richard Feynman. Calculations performed using this method are fully quantum mechanically accurate with no approximations (subject to convergence with respect to well understood parameters and any further approximations and simplification imposed in the simulation).

A variant of PIMD is centroid MD (CMD) which is based upon the centroid

density formulation of path integral quantum mechanics. Of particular use for calculating dynamical properties, this method was thought to be an ideal next-step in the simulation of the Cambridge experimental hydrogen dynamics.

The PIMD code in CASTEP (a popular density functional theory code) is maintained by Dr. Probert of York university. A variant of this code is also kept up to date outside of the CASTEP tree for use with model potential energy surfaces (PESs) and this was used as the computational tool on which an implementation of CMD would be developed and the calculations of H on ruthenium performed.

1.3 Friction - the objective and the benefit

The real objective and aim for this work was to model the ruthenium surface and hydrogen adsorbate in such a way that friction parameters could be determined by fitting the simulated data against that generated by experiment. In so doing, atomic scale, temperature-dependent friction could be explained by a simple model which could elucidate some of the features of the ^3He spin echo results.

The origin of friction on the nano-scale is closely associated with the vibrational modes of the adsorbate on the surface[4]. Kinetic energy of adsorbate atoms can be dissipated by phonons[5], and electrons on metallic surfaces[6]. When an atom is adsorbed on a surface, two types of vibrational mode other than those present in the isolated atom and surface are observed. *Internal modes* arise due to alteration of inter-atomic bonds in the surface layers, and *external modes* because of changes to the atomic motion of the adsorbate in the corrugated potential of the surface. Anharmonic coupling between these modes provides the leading contribution to the dissipation of adsorbate energy on the surface and hence to friction[7].

Atomic scale friction has been studied before [8][9][10] many times, but in many cases the equipment used to measure it was directly involved in the dynamics of the adsorbate. For instance, an atomic force microscope could be used to manipulate an individual adsorbate molecule or atom on the surface, effectively dragging it along some path. This approach can possibly measure the static friction of the adsorbate, but is limited by how fast the AFM probe can be moved. There is also the issue that the friction could be affected by the potential confining the adsorbate to the tip. The advantage of an approach like ^3He spin-echo is that the dynamics are non-destructively (to a large degree) measured with the spatial and temporal resolution to effectively "see"

the dynamics of the adsorbate and infer a friction mechanism.

A simplified PES would be created of hydrogen on ruthenium, upon which CMD wold be performed. These elements, in themselves have no parameters in friction, however, as the molecular dynamics must be performed in the canonical ensemble, where temperature is conserved rather than energy, a Langevin equation was chosen to model the heat-bath. This consists of a frictional damping term and a stochastic "buffeting" term to return energy to the system.

Through the thermostat then, the value of friction in the simulation could be carefully tuned to match experiment.

Chapter 2

Experiment

Interfaces often exhibit very different physical and chemical behaviour than the bulk [11]. This results from the abrupt interaction of solid phase with gas phase or vacuum. In a bulk crystal, the electronic wavefunction may be written in terms of Bloch waves,

$$\Phi_{n,\mathbf{k}} = e^{i\mathbf{k}\cdot\mathbf{r}} u_{n,\mathbf{k}}(\mathbf{r}), \tag{2.1}$$

where $u_{n\mathbf{k}}(\mathbf{r})$ is a wave-like function with the periodicity of the crystal lattice, n is the index of an electronic energy band (band from hereonin) and $\mathbf{k}$ is a wavenumber in the first Brillouin zone. $u_{n\mathbf{k}}(\mathbf{r})$ could for instance be written as a plane wave expansion,

$$u_{n,\mathbf{k}}(\mathbf{r}) = \sum_{\mathbf{G}} c_{n,\mathbf{k}+\mathbf{G}} e^{i\mathbf{G}\cdot\mathbf{r}}, \tag{2.2}$$

so that the wavefunction may be written:

$$\Phi_{n,\mathbf{k}} = \sum_{\mathbf{G}} c_{n,\mathbf{k}+\mathbf{G}} e^{i(\mathbf{k}+\mathbf{G})\cdot\mathbf{r}}. \tag{2.3}$$

$\mathbf{G}$ are the reciprocal lattice vectors, defined with the real-space lattice vectors R, as $\mathbf{G}\cdot\mathbf{R} = 2\pi m$, and the sum runs over all reciprocal lattice vectors.

In a metal, a simple model for the surface states is given when solving the Schrödinger equation for a periodic potential abruptly terminated by a step function,

$$V(z) = \begin{cases} V_p(z), & z < 0 \\ V_0, & z > 0 \end{cases}, \tag{2.4}$$

in 1D, where V_p is the periodic function associated with the bulk and V_0 is the value which the potential decays to in the vacuum as $z \to \infty$. The solutions to

the 1D Schrödinger equation,

$$-\frac{\hbar^2}{2m}\frac{d^2}{dz^2}\Phi(z)+V(z)\Phi(z)=E\Phi(z), \tag{2.5}$$

are given by

$$\Phi(z)=\begin{cases} Au_{-k}e^{-ikz}+Bu_k e^{ikz}, & z<0 \\ Ce^{-\sqrt{2m(V_0-E)}\frac{z}{\hbar}}, & z>0 \end{cases}, \tag{2.6}$$

these are surface Shockley states, with A,B and C, scalar coefficients. It is clear then, that in the bulk, surface states behave as Bloch waves, but outside of the metal interface tail off exponentially. The tail off to constant potential in the vacuum is associated with a dipole field about the domain boundary, resulting from the gradient in charge density it. Because of these effects and others, atoms in the surface region tend to relax into a non-bulk geometry, further affecting the surface physics [12].

Over the last half-century, microscopy techniques have advance to such a degree that the fields associated with individual atoms can be resolved (and manipulated[13]). This has driven and in turn been driven by the development of technologies such as silicon micro-electronics that power the mobile phones, computers and devices so entrenched in modern-day life, the opto-electronics that allow fast, high-bandwidth communication of vast quantities of data worldwide and the medicines which have freed a generation of people from the diseases which afflicted their ancestors since beyond record.

In order to measure effects on such short lengthscales and corresponding quick timescales, a variety of techniques have been employed and are used regularly to measure and characterise a multitude of phenomena. The origins of the field of non-optical microscopy go back to x-ray crystallography, first pioneered in the 1910s. The technique has been used to probe the nature of chemical bonds, atomic size, but in particular, the structure of crystals and organic molecules.

Many techniques, including Atomic Force Microscopy (AFM) and x-ray crystallography are used to measure static phenomena on atomic length scales, however, these techniques can be roughly divided into two categories; those which are better suited to studying the bulk, such as x-ray crystallography, and those which are more naturally employed to examine surfaces, such as AFM. When studying dynamics, such as diffusion processes of introduced impurities, this division is also apparent. In the 1970s, a technique known as Neutron spin-echo interferometry was developed which is capable of measuring dynamical processes in materials. As neutrons can penetrate deep into a surface, however, this technique was not a good approach for measuring surface dynamics, such as adsorbate diffusion.

2.1 He-3 Spin-Echo Spectroscopy

Surface states can be probed continuously and non-invasively with helium-3 scattering experiments; ^{3}He atoms are inert and when incident on a surface are reflected roughly 3.6Å above the surface due to electronic interactions.[14]

Quasi-elastic helium atom scattering can be used to measure dynamics of adsorbates on surfaces through the energy transfer between the beam and the surface states. Incident ^{3}He atoms will scatter elastically from static surfaces, but when the adsorbate is moving on the surface, the elastic peak in energy of the reflected beam will be broadened with respect to the incident energy distribution, due to a quantum mechanical analogue of the Doppler effect.

Initial experiments were performed for ^{3}He scattering from surfaces in the 1970s, where time of flight measurements were made. In this approach, collimated beams of ^{3}He atoms have their velocity distribution measured prior to and subsequent to scattering with the surface, giving a measurement for the energy transferred to the surface from the beam. In such experiments, the precision of measurement of the time of flight from the beam generator to the detector is of crucial importance to the accuracy of the technique and is the major difficulty in implementing such a system. It has been found [15] that the energy resolution of time of flight measurements is limited to 0.3meV by the velocity spread of the beam and uncertainty in the timing of the particle flight.

In contrast to a direct time of flight measurement, the Cambridge surface physics group has constructed a ^{3}He spin-echo interferometer. This equipment effectively uses a magnetic field to temporally split a polarised wave-packet of ^{3}He, before it scatters from the surface, at which point an equal and opposite magnetic field is used to recombine the reflected wave-packets. This allows for the imposed spin components of the ^{3}He wave-packets to be used as timers for their own trajectory.

The ^{3}He spin-echo measurement gives a change in polarisation of the beam as a function of time, which is equivalent to directly measuring the intermediate structure factor (ISF). It is worth noting at this point that the ISF, written $F(\Delta\mathbf{k},t)$ is related to the Van-Hove generalised pair correlation function, $G(\mathbf{r},t)$ and the dynamic structure factor, $S(\Delta\mathbf{k},\omega)$ through spatial and temporal Fourier transforms as follows[11],

$$G(\mathbf{r},t) \underset{SpatialFT}{\Longleftrightarrow} F(\Delta\mathbf{k},t) \underset{TemporalFT}{\Longleftrightarrow} S(\Delta\mathbf{k},\omega) \tag{2.7}$$

The most intuitively simple of these representations is the Van-Hove function.

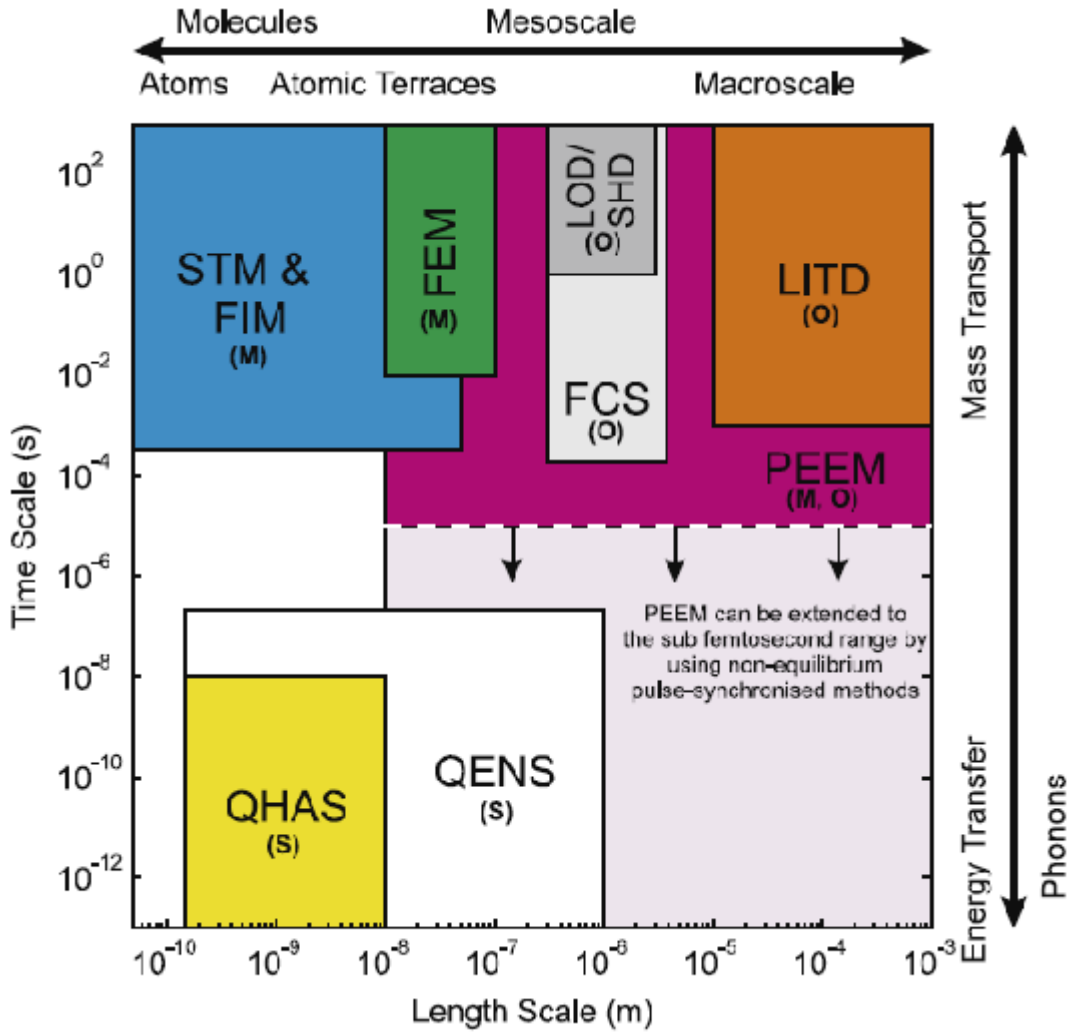

Figure 2.1: An approximate visual guide to the spatial and temporal resolution of commonly applied surface sensitive measurement techniques (figure taken from Jardine *et al*[1]). The letters in parentheses indicate the category of experiment to which the techniques belong; where O stands for optical or laser based; M, microscopic imaging and S, scattering methods. Quasi-elastic ^3He atom scattering (QHAS), which includes ^3He spin-echo is the only method currently available for studying sub-nanosecond timescales at atomic length-scales. Quasi-elastic neutron scattering (QENS) is included for the sake of comparison, and is not strongly surface sensitive.

This is defined in real space and time as:

$$G(\mathbf{r},t) = \langle \frac{1}{N} \int \sum_{i=1}^{N} \sum_{j=1}^{N} \delta(\mathbf{r}' + \mathbf{r} - \mathbf{r}_j)\delta(\mathbf{r}' - \mathbf{r}_i(0))d\mathbf{r}' \rangle, \tag{2.8}$$

this can be best explained after splitting the expression into a self-part and a distinct-part. So that,

$$G(\mathbf{r},t) = G_s(\mathbf{r},t) + G_d(\mathbf{r},t), \tag{2.9}$$

where the self-part, G_s gives the probability of a particle having moved a dis-

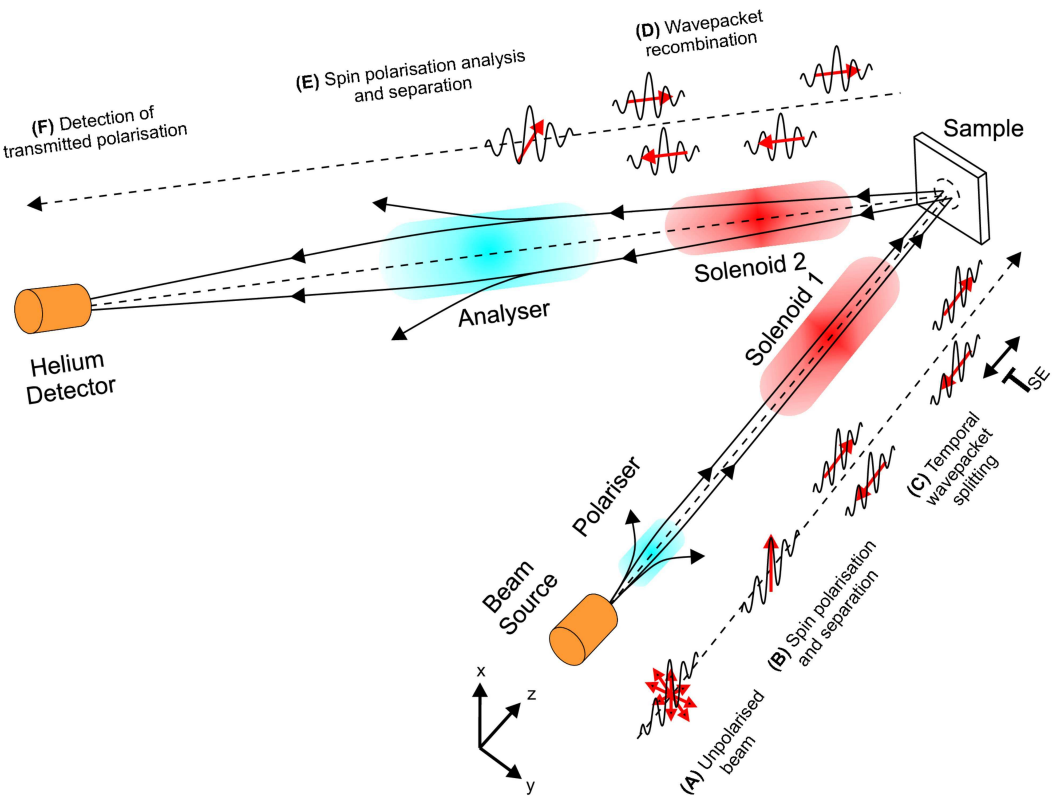

Figure 2.2: This figure, from Jardine *et al*[2] shows a schematic of the Cambridge ^3He spin-echo interferometer. A beam of ^3He atoms is generated at A, it is then collimated at B so that the nuclear spin of the atoms is perpendicular to the beam, before passing through a magnetic field at C which splits the wave-packets into a super-position of wave-packets with nuclear spin parallel and antiparallel to the direction of the beam. The second of these components reaches the surface at a time delay δt with respect to the first. After reflection the wavepackets are recombined by an equal but opposite magnetic field at D; if the surface has changed in δt then the recombined wave-packet will have a spin rotated in the $x-y$ plane with respect to the original orientation. This gives the analogue of measuring the time of flight of the scattering process in more traditional scattering experiments. Finally at E, single spin components are selected at a time to be deflected into the mass-spectrometer type detector at F, where the count rate gives the intensity of the transmitted polarisation.

tance $\mathbf{r}$ in time t and the distinct part, G_d gives the probability that there is a particle at a distance $\mathbf{r}$ from a coordinate at which, at $t = 0$, there was a *different* particle.

In order to calculate ISFs from simulation, there is clear route from a trajectory, through a discretised Van-Hove function on a grid and a spatial Fourier transform to an ISF.

In practice, however, there is a formidable barrier to performing the calculation this way, as G must be defined on a fine grid (in 3D), which may have enough points that it is computationally infeasible to take its Fourier trans-

form. Furthermore, since the experimental data is measured only along particular azimuths, for certain discrete values of momentum transfer, a majority of the data calculated in this way will be useless for comparison with experiment. An alternative is to calculate ISFs directly by recognising that (2.8) can be written in terms of microscopic densities as

$$G(\mathbf{r},t) = \langle \frac{1}{N} \int \rho(\mathbf{r}'+\mathbf{r},t)\rho(\mathbf{r}',0)d\mathbf{r}' \rangle. \tag{2.10}$$

This allows for the recognition that the ISF,

$$F(\mathbf{k},t) \equiv \int G(\mathbf{r},t)e^{-i\mathbf{k}\cdot\mathbf{r}}d\mathbf{r}, \tag{2.11}$$

is independent of integration order, so can equivalently be written as

$$F(\mathbf{k},t) = \langle \frac{1}{N}\rho(\mathbf{k},t)\rho(-\mathbf{k},0) \rangle, \tag{2.12}$$

where ρ are microscopic densities, or the Fourier components of density. Writing the ISF in this way allows for direct calculation of the ISF for particular momentum transfer as the autocorrelation of $e^{i\Delta\mathbf{k}\cdot\mathbf{r}}$ if the system has time reversal symmetry[16].

2.2 Hydrogen on ruthenium - sites, energy differences, diffusion rates

The Cambridge surface physics group has compiled a set of data for hydrogen adsorbates on ruthenium surfaces, in particular the (0001) cleavage, which has hexagonal geometry. Ruthenium is an HCP transition metal, with average atomic weight of 101.07 amu; its structure is given in figure 2.3.

On the HCP(0001) surface are two types of hollow sites, termed HCP and FCC hollow sites. These sites do not differ in the surface layer of atoms, they are both equidistant from 3 surface atoms, but instead in the layer directly beneath. Directly under the HCP site is an atom in this layer, whereas in the FCC site there is none. They are named in such a way because if the surface was continued in the **c** direction (see figure 2.3), so that another surface layer was laid on top, the HCP sites would be those above which the new atoms would reside if the layering was continued in an HCP fashion, whereas the concept for the FCC sites is the same, but where the stacking arrangement is changed to FCC[17].

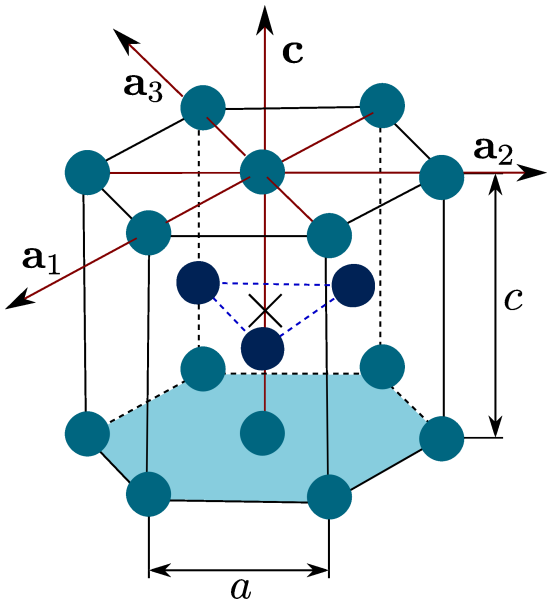

Figure 2.3: Ruthenium is an HCP metal and can be described in terms of the basis vectors and lattice parameters outlined above. The Ruthenium atoms are represented by blue circles, with the *Ru* atoms of the central plane highlighted in dark-blue. The cross shows the centroid of the central plane and of the cell. The light blue hexagon shows part of the (0001) plane, which is the cleavage on which the surface adsorbate diffusion is conducted..

2.3 Experimental Parameters

2.4 Measured quantities

ISFs are measured directly from the ^3He spin-echo experiment. Both the real and imaginary components are measured, though it is expected that the Van-Hove function will be symmetric in both space and time for aperiodic diffusion, hence the dynamic structure factor will be symmetric about zero energy transfer (no net energy transfer). It is then reasonable to assume from this that when Fourier transforming back to the time domain, to an ISF, that the imaginary part will be zero. [16]

2.4.1 Intermediate Structure Factor Analysis

The ISF itself represents the time dependence of the correlation of the atomic configuration for those atoms under consideration for the length-scale and direction defined by $\Delta\mathbf{k}$ [1]. While the Van-Hove function is more intuitively understood, mapping models from that representation to yield analytic forms for the ISF is difficult as the N-dimensional Fourier transform gets in the way.

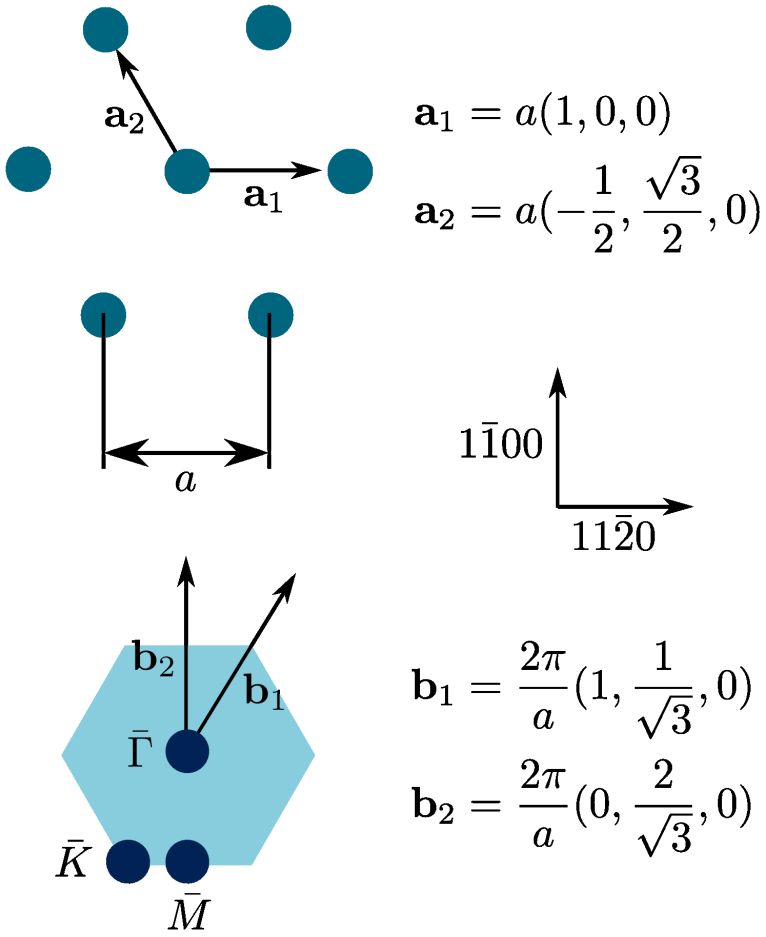

Figure 2.4: The HCP(0001) surface is represented schematically with in-plane lattice vectors shown as $\mathbf{a}_1$ and $\mathbf{a}_2$. The high-symmetry directions, $\langle 1\bar{1}00\rangle$ and $\langle 11\bar{2}0\rangle$ are shown, which are also the nearest-neighbour and next-nearest neighbour interstitial site directions. Finally, the reciprocal space lattice vectors are shown as $\mathbf{b}_1$ and $\mathbf{b}_2$ on the first Brillouin zone, depicted in light blue, with three high-symmetry $\mathbf{k}$-points highlighted.

Models are necessary, however, in order to characterise the behaviour of the adsorbate motion.

If the scattering atoms undergo simple diffusion (that is, their mean-square displacement is proportional to time,

$$\langle \Delta\mathbf{r}(t) \cdot \Delta\mathbf{r}(t) \rangle = 2NDt, \tag{2.13}$$

where N is the dimensionality of the problem, then the ISF assumes an expo-

nential form [18] such as:

$$F(\Delta\mathbf{k},t) = I_0 e^{-\alpha t}, \tag{2.14}$$

where α is the dephasing rate. The variation of the dephasing rate with momentum transfer characterises the mechanism of diffusion. Several simple models can be constructed to help with the characterisation, for instance; Brownian motion yields a quadratic variation[1], whereas hopping between energy minima on a Bravais lattice is given by the Chudley-Elliot model[19], finally ballistic motion is known to have a Gaussian Van-Hove function, which of course remains Gaussian through the Fourier transform to an ISF. The forms for these three models is given in table 2.1

Mechanism	Form of $\alpha(\Delta\mathbf{k})$
Brownian	$D\Delta\mathbf{k}^2$
Chudley-Elliot Hopping	$2\sum_j \nu_j sin^2\left(\frac{\Delta\mathbf{k}\cdot\mathbf{l}_j}{2}\right)$
Ballistic	$\sqrt{\frac{2ln(2)k_BT}{m}}\Delta\mathbf{k}$

Table 2.1: Table giving the analytical dependence on momentum transfer of dephasing rate (α) for three simple mechanisms of diffusion. In the Chudley-Elliot mechanism ν_j are the jump frequencies and $\mathbf{l}_j$ are the jump vectors possible in the Bravais lattice, indexed by j.

2.4.2 $\alpha(\Delta k)$ plots

While ISFs are measured directly by the experimental technique, the results from a set of ISFs at various momentum transfers can be compactly represented by an $\alpha - \Delta k$ plot. Since diffusion processes are represented by exponentials in the ISF, models involving a sum of exponentials,

$$F_{\mathbf{k}}(t) = ae^{-\alpha t} + be^{-\beta t} + c, \tag{2.15}$$

where α and β are the dephasing rates of two surface decays, match the profile of the data. In the experimental set of measured ISFs, much of the data cannot be fitted successfully with one exponential contribution, whereas two are all that is necessary for a good fit (see figure 2.5). This suggests that depending on the temperature, azimuth and magnitude of momentum transfer, either 1 or 2 decay processes are observed.

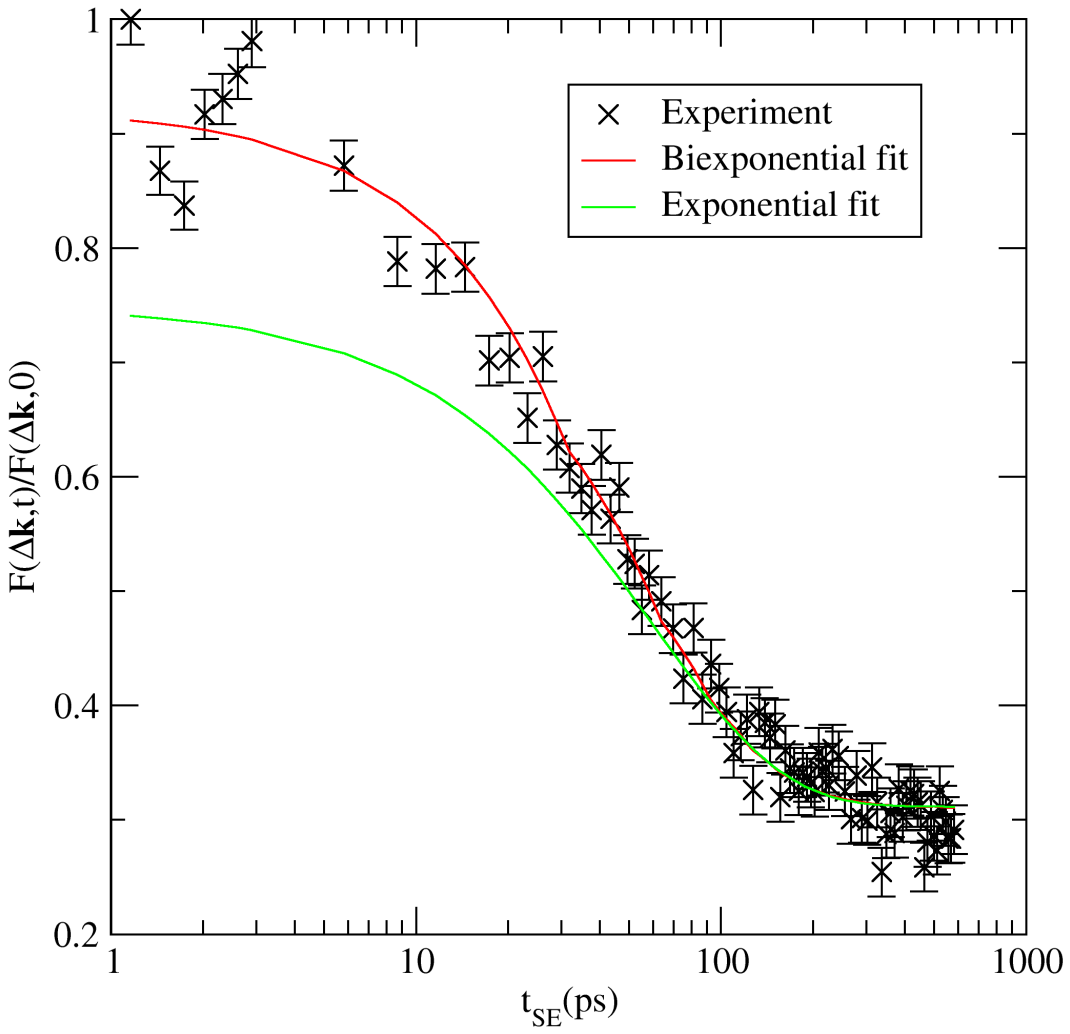

Figure 2.5: An example of experimental ISF data along the $\langle 11\bar{2}0 \rangle$ azimuth at a temperature of 250K and momentum transfer magnitude of $\Delta k = 1,76\mathring{A}^{-1}$. Two fits are presented alongside the data; a single exponential fitted to the long-time data and a two-exponential model. The time axis is logarithmic and the data is courtesy of Eliza McIntosh.

2.5 Adsorbate density and Fermionic Hydrogen

It is important to note that the surface coverage of hydrogen on the surface is approximately 0.2 mololayers (ML). This has implications for the calculation of the behaviour of the adsorbate, as the proton of the hydrogen nucleus is a Fermion, whereas the proton-electron system which makes up the atom is a composite Boson at high enough temperature. The expectation of the experimental group was that a Bosonic treatment of the Hydrogen would be applicable, as the packing density is so low and electronic structure calculations [20] suggest that the electronic density of the hydrogen is localised to the nucleus and correlated with its motion. For this reason, together with further discussion in chapter 3, the adsorbate was treated Bosonically in this work, though

Fermi-Dirac statistics have been investigated.

Chapter 3

Theory

3.1 Molecular Dynamics

Molecular dynamics is the computational simulation of the movement of classical physical particles, by solving Newton's equations (3.1) numerically in a potential field. It has historically been used most often to calculate macroscopic properties through ensemble averages. While the idea is simple, there are various subtleties which have been studied in depth over the latter half of the 20th century. For a system of N particles in a potential, the classical equations of motion can be written,

$$\begin{aligned} \mathbf{F}_i &= m_i \mathbf{a}_i, \\ m_i \frac{d^2 \mathbf{r}_i}{dt^2} &= -\frac{dV}{d\mathbf{r}_i}, \end{aligned} \tag{3.1}$$

where V is the external potential in the system. Energy conservation is implied as there is no dissipative term and any numerical integration (finite difference) method may be employed to evolve the positions of the particles in time. As time is necessarily quantised for representation computationally and due to the finite order of integration algorithms, the trajectories obtained by numerically integrating these equations of motion will always diverge from the true trajectory in the long term limit. For dynamical observables, either an integrator must be chosen with a high enough order, or a short enough time quantisation chosen that trajectories are exact to some arbitrary tolerance for run-times comparable to the correlation time of the observable. Often, however, exact trajectories are not necessary, as we actually want use the approach to sample states from the Microcanonical ensemble; in this case the criteria can be relaxed to energy conservation only. Integration algorithms are sensitive to fast movement, and may diverge with an inappropriately long time-step for

the speed of the motion. For this reason it is important that a suitably short time-step is chosen, particularly when the system is given a large energy or with low-mass particles. Calculating potentials are also, often expensive, so typically an integrator with few potential evaluations is chosen. This usually rules out the oft- employed finite-difference methods for ordinary differential equations, such as Runge- Kutta methods. Needing a high enough order for accurate trajectories, then leads to a compromise; the Velocity Verlet method has $O(\Delta t^2)$ error in both position and velocity and has become the standard in molecular dynamics, partly because it requires only one potential evaluation per cycle to achieve this accuracy.[21] The algorithm can be written as:

Algorithm 1 Velocity Verlet Algorithm

Function $f : \mathbb{R}^n \to \mathbb{R}^n, \quad \mathbf{v}(t) \mapsto \mathbf{v}(t+\Delta t)$

$$\begin{aligned}
\mathbf{v} &\to \mathbf{v} + \frac{1}{2}\mathbf{a}\Delta t \\
\mathbf{x} &\to \quad \mathbf{x} + \mathbf{v}\Delta t \\
\mathbf{a} &= \quad -\frac{1}{m}\frac{dV}{d\mathbf{r}_i} \\
\mathbf{v} &\to \mathbf{v} + \frac{1}{2}\mathbf{a}\Delta t.
\end{aligned}$$

End Function

3.2 Path Integrals

In Lagrangian classical mechanics, the principle of least action states that the change in the action,

$$\mathscr{S} = \int_{t_0}^{t_1} \mathscr{L}(\dot{\mathbf{q}}(t), \mathbf{q}(t), t)dt, \tag{3.2}$$

where $\mathscr{L}$ is the Lagrangian of the system, is zero along the path in configuration space which would be taken physically by the system evolving from its configuration at t_0 to that at t_1 [22].

It was shown by Feynman that an analogous concept exists in quantum mechanics [23]. Starting from the concept of the time-evolution operator $\hat{U}$ in the Heisenberg picture of quantum mechanics, the Green's function of the time-dependent Schrödinger equation, or the *propagator* can be written

$$K(x,t,x_0,t_0) = \langle x|\hat{U}(t,t_0)|x_0\rangle, \tag{3.3}$$

which can be used to evolve a state through an interval in time,

$$\psi(x,t) = \int K(x,t,x_0,t_0)\psi(x_0,t_0)dx_0. \tag{3.4}$$

$$K(x,t,x_0,t_0) = ae^{-i\mathscr{S}/\hbar} \tag{3.5}$$

For short timesteps, the action may be approximated as

$$\mathscr{S} = \int_{t_0}^{t_1} \mathscr{L}dt = \langle \mathscr{L}\rangle \Delta t, \tag{3.6}$$

to first order, where Δt is the timestep, $t_1 - t_0$ and $\langle \mathscr{L}\rangle$ is the average Lagrangian over this period. With these results, it is possible to claim that a finite propagation in time may be represented by the serial application of the approximate propagator;[24]

$$K(x_{final},t_{final},x_{initial},t_{initial}) = \int \prod_{i=1}^{N-1} dx_i e^{i\sum_{i=1}^{N-1}\mathscr{L}(t_i)\Delta t/\hbar} \tag{3.7}$$

Classically, a system evolves from one state to another along the path in configuration space, $\delta\mathscr{S} = 0$; the quantum mechanical propagator (3.7) can be interpreted as an integral over all paths in phase space. This idea ties in neatly with the double-slit experiment, as rather than the incident particle "weirdly" passing through both slits, it can be seen from the path-integral propagator that an unimpeded, *quantum mechanical* particle would explore every possible path. In the double-slit experiment, most paths have been blocked, leaving only two possible routes to the screen, but both of them are dutifully explored!

3.2.0.1 Derivation

More formally, the path integral representation of quantum mechanics can be derived by firstly taking the density as written using the canonical Boltzmann operator,

$$\rho(\beta) = e^{-\beta\mathscr{H}}, \tag{3.8}$$

where thermodynamic $\beta = 1/T$ and the Hamiltonian, $\mathscr{H}$ is of the usual form,

$$\mathscr{H} = \mathscr{T} + \mathscr{U}, \tag{3.9}$$

and the kinetic $\mathscr{T}$ and potential $\mathscr{U}$ energy operators do not commute,

$$[\mathscr{T}, \mathscr{U}] \neq 0. \tag{3.10}$$

The partition function can be written,

$$Z(\beta) = Tr(e^{-\beta\mathscr{H}}), \tag{3.11}$$

where Tr represents the trace, or alternatively in path-integral form can be written as

$$\begin{aligned} Z(\beta) &= \int dq \langle q|e^{-\beta(\mathscr{T}+\mathscr{U})}|q\rangle & (3.12)\\ &= \lim_{P\to\infty} \int dq \langle q|A^P|q\rangle, & (3.13) \end{aligned}$$

where A is expressed as:

$$A = e^{-\frac{\beta}{2P}\mathscr{U}} e^{-\frac{\beta}{P}\mathscr{T}} e^{-\frac{\beta}{2P}\mathscr{U}}, \tag{3.14}$$

by Trotter's theorem. It should be noted that this step is necessary because $\mathscr{T}$ and $\mathscr{U}$ do not commute (3.10). Taking the identity relations,

$$\begin{aligned} \mathbf{I} &= \int dq|q\rangle\langle q| & (3.15)\\ \mathbf{I} &= \int dp|p\rangle\langle p|, & (3.16) \end{aligned}$$

a full set of position and momentum states is introduced. Firstly it is noted that the integrand in (3.12) can be written,

$$\langle q_1|A^P|q_1\rangle = \langle q_1|A|q_2\rangle\langle q_2|A|q_3\rangle\langle q_3|\cdots|q_P\rangle\langle q_P|A|q_1\rangle, \tag{3.17}$$

using the set of position states. Where q has become q_1 to simplify the indexing. So that

$$Z(\beta) = \lim_{P\to\infty} \int_{q_{P+1}=q_1} \prod_{i=1}^{P} dq_i \langle q_i|A|q_{i+1}\rangle. \tag{3.18}$$

Substituting for A, it can be seen that

$$\langle q_i|A|q_{i+1}\rangle = \langle q_i|e^{-\frac{\beta}{2P}\mathscr{U}}e^{-\frac{\beta}{P}\mathscr{T}}e^{-\frac{\beta}{2P}\mathscr{U}}|q_{i+1}\rangle \tag{3.19}$$

$$= e^{-\frac{\beta}{2P}(\mathscr{U}(\mathbf{q}_i)+\mathscr{U}(\mathbf{q}_{i+1}))}\langle q_i|e^{-\frac{\beta}{P}\mathscr{T}}|q_{i+1}\rangle, \tag{3.20}$$

in the limit of large P, as:

$$e^{A+B} = e^A e^B(1-\frac{1}{2}[A,B]+\mathscr{O}(N^3)), \tag{3.21}$$

and so β/P must be small as this is only correct up to the linear term, as it has been stated (3.9) that $\mathscr{U}$ and $\mathscr{T}$ do not commute. Focussing on the remaining terms, and using a set of momentum states from (3.15),

$$\langle q_i|e^{-\frac{\beta}{P}\mathscr{T}}|q_{i+1}\rangle = \int dp\langle q_i|p\rangle\langle p|e^{-\frac{\beta}{P}\mathscr{T}}|q_{i+1}\rangle \tag{3.22}$$

$$= \int dp e^{-\frac{\beta p^2}{2Pm}}\langle q_i|p\rangle\langle p|q_{i+1}\rangle. \tag{3.23}$$

Using the result,

$$\langle q|p\rangle = \frac{1}{\sqrt{2\pi\hbar}}e^{ipq/\hbar}, \tag{3.24}$$

the expectation value can be written,

$$\langle q_i|e^{-\frac{\beta}{P}\mathscr{T}}|q_{i+1}\rangle = \int dp e^{-\frac{\beta}{2mP}p^2}e^{ip(q_i-q_{i+1})/\hbar} \tag{3.25}$$

$$= \sqrt{\frac{mP}{2\pi\beta\hbar^2}}e^{-\frac{mP}{2\beta\hbar^2}(q_i-q_{i+1})^2} \tag{3.26}$$

So that, assembling these results,

$$\langle q_i|A|q_{i+1}\rangle = \sqrt{\frac{mP}{2\pi\beta\hbar^2}}e^{-\frac{mP}{2\beta\hbar^2}(q_{i+1}-q_i)^2-\frac{\beta}{2P}(\mathscr{U}(q_i)+\mathscr{U}(q_{i+1}))}. \tag{3.27}$$

Then, the partition function can be written in path integral form as

$$Z(\beta) = \lim_{P\to\infty}\frac{mP}{2\pi\beta\hbar^2}^{P/2}\int_{q_1=q_{P+1}}\prod_{i=1}^{P}dq_i e^{-\beta V}, \tag{3.28}$$

where

$$V = \sum_{i=1}^{P}\frac{mP}{2\beta\hbar^2}(q_{i+1}-q_i)^2+\frac{1}{P}\mathscr{U}(q_i). \tag{3.29}$$

Here, any operators have disappeared and the equation is entirely in terms of a set of augmented positions and momenta. Written with reference to Mosel [25].

3.2.1 Ergodic Principle

In statistical mechanics, ensemble average quantities can be calculated by summing over the microstates of the system with the appropriate partition function. This is somewhat removed from how (path-integral) molecular dynamics operates and a more obvious fit for calculating such properties would be a Monte-Carlo simulation. Ensemble averages can be calculated with molecular dynamical techniques, by making use of the ergodic principle and Liouville's theorem[26]. One way of stating the ergodic principle is that a fair estimator will sample all of configuration (or phase) space, and hence microstates in the limit of large time. This is important because it implies that a time averaged quantity in molecular dynamics is equivalent to a thermodynamic ensemble average. Liouville's theorem allows that sampling along a trajectory in a system, in time, can be equivalent to sampling from the thermodynamic ensemble, so long as that trajectory was propagated under the same ensemble. This is because, according to the theorem, locally, the density of microstates in a system is constant in such a case. This is important because the system must be locally at equilibrium in order that the equilibrium properties of the system be fairly sampled.

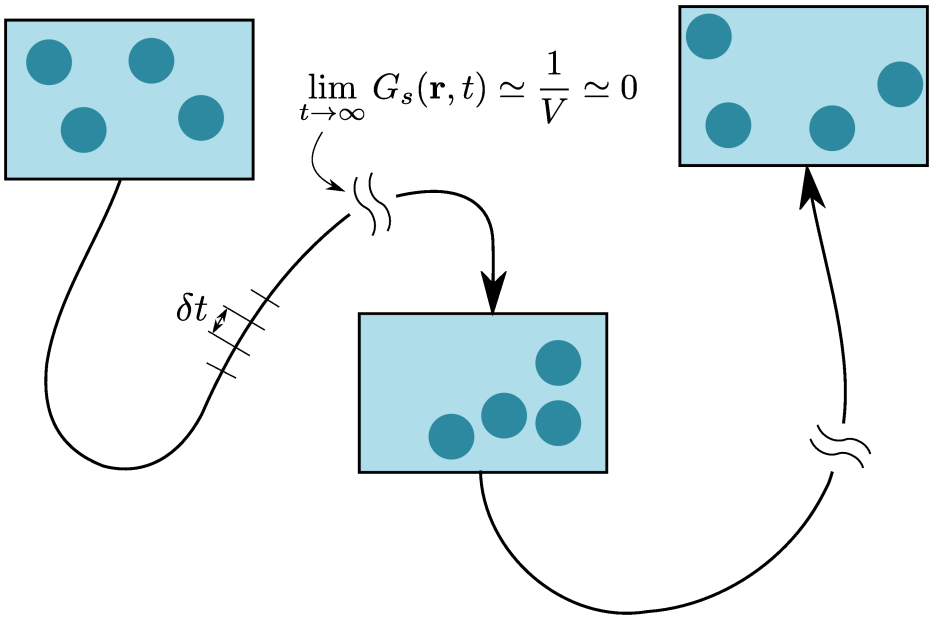

Figure 3.1: The ergodic principle together with Liouville's theorem allow for the calculation of thermodynamic ensemble averages to be calculated as time averages of the system evolved in the appropriate ensemble in the limit of long time and for sufficiently short time-step. This approach can also be used to find another initialisation for a simulation, as in the limit of long time, the system in its final and initial states will become uncorrelated; so that the self part of the Van-Hove function, G_s goes to zero.

3.3 Path Integral Molecular Dynamics

Path integral Molecular dynamics was first proposed in 1981[27], it was initially meant to be used as a more efficient way to perform the integral in (3.28) (than Monte-Carlo methods). The idea is simply to take note that the effective potential (3.29) has a classical isomorphism which is a set of particles connected by springs, as evidenced by the harmonic terms in the expression. This classical system can be propagated in time with standard molecular dynamics techniques and by the ergodic principle, time averages will be equivalent to ensemble averages in the limit of large time[28].

Starting from the partition function;

$$\mathscr{Z} = \sum_j e^{\beta E_j} = \int dx \langle x | e^{-\beta \mathscr{H}} | x \rangle, \tag{3.30}$$

where thermodynamic $\beta = 1/k_B T$, and knowing that matrix elements can be calculated in the path integral formalism.

$$Z = \int \mathscr{D}x(\tau) e^{-\frac{1}{\hbar}\oint \mathscr{H} d\tau}, \tag{3.31}$$

where $\tau = it$, or imaginary time, as in the comparison of $e^{\beta\mathscr{H}}$ with the time evolution operator (3.5), it can be seen that $t = -i\hbar\beta$. e^{ix} is of course cyclic, so hence the imaginary time evolution operator is also.

Path integral Molecular dynamics (PIMD) is derived by noticing that a trotter factorisation,

$$e^{A+B} = \lim_{N\to\infty} (e^{A/N} e^{B/N})^N, \tag{3.32}$$

may be applied to the matrix, $e^{\beta\mathscr{H}}$, if $\mathscr{H}$ is written as $K+V$, so that the partition function becomes:

$$Z_N = \left(\frac{mN}{2\pi\beta\hbar^2}\right)^{N/2} \int \cdots \int dx_1 \cdots dx_N e^{-\beta \frac{mN}{2\beta^2\hbar^2} \sum_{t=1}^{N} (x_t - x_{t+1})^2 + \frac{1}{N}\sum_{t=1}^{N} V(x_t)}, \tag{3.33}$$

so that in the limit of $N \to \infty$, the partition function converges to the exact result. Furthermore, if the integrand is viewed as a propagator in time, then the N variables could be propagated with a molecular dynamics approach, with the potential,

$$\Phi_N(x_1 \cdots x_N; \beta) = \frac{mN}{2\beta^2\hbar^2} \sum_{t=1}^{N} (x_t - x_{t+1})^2 + \frac{1}{N}\sum_{t=1}^{N} V(x_t). \tag{3.34}$$

Of course, this could never be achieved with an infinite number of variables,

but rather quantities would be converged to arbitrary precision by increasing N. In this approach, it is also clear that the potential leads to a nice isomorphism, as the first term is a series of harmonic interactions between variables; a molecular dynamics simulation of a ring of beads, connected by springs is enough to simulate the quantum mechanical propagation of a particle through a potential, V. This is known as PIMD.

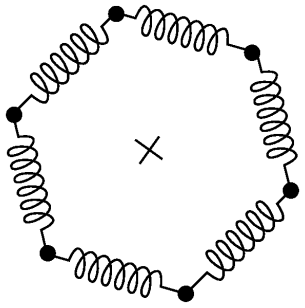

Figure 3.2: The classical isomorphism of the discretised path integral is the bead-spring system whereby a ring of fictitious particles connected by springs is propagated in time. In so doing fully accurate quantum mechanical results can be achieved in the limit of large number of beads and long time. The centre of mass, or "centroid" of the bead-spring system is shown with an x.

3.4 Thermostatting

As discussed earlier, molecular dynamics samples the microcanonical ensemble; this is true for both the classical and path integral cases. In reality, however, it is more common to have a system coupled to a heat-bath which conserves temperature, rather than energy. In order to sample from a canonical ensemble in a molecular dynamics simulation, this heat-bath must be replicated somehow. Doing so in order to constrain the temperature to a set value is known as thermostatting.

3.4.1 Langevin Thermostat

The idea behind this thermostat is to model the heat-bath with the Langevin equation,

$$\mathbf{F}_i = \gamma \mathbf{p}_i + \sqrt{\frac{2\gamma M_i}{\beta}} \mathbf{x}_i, \tag{3.35}$$

the two terms in the Langevin equation correspond to drift and diffusion, respectively. Where the particles are indexed by i and γ represents the friction

coefficient. The Langevin equation models a particle moving in a sea of others. The drift term scales its velocity in accordance with some friction parameter, whereas the diffusion term adds an appropriate stochastic contribution to the velocity which keeps the temperature of the system at a pre-defined value, to represent a Brownian contribution to the motion. Usually, the Langevin thermostat is used only in the calculation of time-averaged properties, as the diffusion term alters short-term dynamical information of the particle in the potential field. In this case, as the Langevin thermostat will fix the temperature regardless of the value of the friction parameter, it is used solely to tune the efficiency of the sampling of phase- space.

3.5 The Centroid in Path Integrals

Like the path integral formulation, the path centroid is also an idea profilated by Richard Feynman. Interestingly this quantity has been shown to play a central role in the correspondence of quantum and classical quantities[29]. The centroid represents the imaginary time average of a closed Feynman path, which corresponds to the zero-frequency Fourier mode of that path.[3]

$$\mathbf{q}_0 = \frac{1}{\hbar\beta}\int_0^{\hbar\beta} d\tau \mathbf{q}(\tau) \tag{3.36}$$

Feynman notes that the path integral formalism can be cast in terms of this centroid variable, by defining another quantity, the centroid density, given by

$$\rho_c(\mathbf{q}_c) = \int\cdots\int \mathscr{D}\mathbf{q}(\tau)\delta(\mathbf{q}_c - \mathbf{q}_0)e^{-\mathscr{S}[\mathbf{q}(\tau)/\hbar]} \tag{3.37}$$

where $\mathbf{q}$ again represents a position in space, and $\mathbf{q}_0$ the centroid of one of the particular paths in the integrand, except that $\delta(\mathbf{q}_c - \mathbf{q}_0)$ will be zero if $\mathbf{q}_c \neq \mathbf{q}_0$. Hence, the integral is constrained to be over those paths for which the centroid is at $\mathbf{q}_c$. In order to recover the partition function, the centroid density must be integrated over all possible centroid positions:

$$Z(\beta) = \int dq_c \rho_c(\mathbf{q}_c) \tag{3.38}$$

While Feynman and Kleinart showed that casting the path-integral formulation of quantum mechanics in terms of the centroid density is a useful way to extract classical observables from quantum mechanical systems[30], it was Cao and Voth that rigorously showed that Boltzmann statistical mechanics can be written in terms of the centroid density[31]. In this formulation, the cen-

troid density plays the same role as probability density in classical statistical mechanics.

While as applicable to the calculation of equilibrium properties as the standard path- integral formulation, the centroid density approach is of particular merit when applied to dynamical properties, as shown in the companion paper to that referenced above, Cao and Voth go on to explain how the centroid-density formulation can be used to calculate time-correlation functions on realistic time-scales and ultimately describe what they call *Centroid Molecular Dynamics* (CMD)[31].

3.6 Centroid Molecular Dynamics

Time correlation functions are fundamental quantities in classical mechanics, and it is perhaps not initially obvious how to generalise such a concept to quantum mechanics; especially those requiring definite positions and momenta at particular times. That is not to say that a time correlation function could not be defined on the expectation value of position and momentum for a quantum system. In such a case, while the expectation values are quasi-classical quantities, it is entirely reasonable to suggest that as the dynamical equations of motion of the system are quantum mechanical, the trajectory of $\langle x \rangle$ and $\langle p \rangle$ will reflect this and present qualitatively different correlation profiles, evidencing a "quantum correction" to the classical dynamics.

The obvious simplification and approximation here is that the fully quantum mechanically accurate system is not bound to follow a trajectory of the expectation value of position and momentum.

The problem with PIMD in its usual formulation, when considering dynamics, is that the beads and bead trajectories present fictitious information about the time evolution of the system, despite often giving believable results. PIMD has a well established history in the calculation of ensemble averages, but the beads and bead trajectories were viewed more as a phase space sampling device and the non-physical path through this space with no meaning outside of ensemble averages. In essence, the sum over the beads represents the discretised, imaginary-time integral over a single Feynman path, whereas the evolution in time of the bead-spring system represents the integration over Feynman paths. Together, these two procedures can be employed to sample phase space efficiently and present accurate, ensemble-averaged quantities, when run for sufficient time and with enough beads, by the ergodic principle.

In effect, if we are looking for the dynamics, the problem is that the inte-

grals in time and phase space are not necessarily in the correct order. Ensemble average quantities are invariant under a change of sampling order, hence why path-integral Monte-Carlo methods can work. So, another way of looking at this is that while the bead-spring system is in a particular state, the Feynman-paths which are in some sense *at* this location in phase space, should be summed over first, followed by subsequent points in phase space, to form a trajectory.

As we are looking for expectation values, this can be shown to be the centroid, or centre of mass of the bead-spring system in the ring-polymer isomorphism. Importantly Feynman suggests a modification to the path integral formulation of quantum mechanics, in terms of the centroid.

Centroid MD was first proposed by Cao and Voth in the first and second of a series of manuscripts published in 1994[31]. It is often thought of as a way to simulate the dynamics of quantum mechanical systems on realistic timescales. More formally it is a procedure by means of which Kubo-transformed time-correlation functions can be generated for the system under study.

Starting again from the partition function, but the centroid-density split version in eq.(3.38), if we were now to discretise the action integral of this partition function in the same way as for the equilibrium (non-centroid density) case, then ρ_c becomes

$$\rho_c(\mathbf{q}_c) = \frac{mP}{2\pi\hbar^2\beta}\int \mathscr{D}\mathbf{q}\,\delta(\mathbf{q}_c - \mathbf{q}_0)e^{-\sum_{i=1}^{P}(\frac{mP}{2\hbar^2\beta}(\mathbf{q}_i-\mathbf{q}_{i+1})^2+\frac{\beta}{P}V[\mathbf{q}_i])} \tag{3.39}$$

Then the equations of motion are constructed so that the centroid variable moves in a potential of mean force generated by a sum over paths with the same centroid, given by [32]

$$V_c(\mathbf{q}_c) = -\frac{1}{\beta}ln(\rho_c(\mathbf{q}_c)), \tag{3.40}$$

and the equations of motion are:

$$\frac{dq_c(t)}{dt} = \frac{1}{m}\mathbf{p}_c(t) \tag{3.41}$$

$$\frac{dp_c(t)}{dt} = \mathbf{F}_c(\mathbf{q}_c(t)) \tag{3.42}$$

where p_c is the momentum of the of the centroid position, x_c. Initial conditions for the centroid molecular dynamics should be sampled from the phase space

centroid distribution [33],

$$\rho_c(\mathbf{q}_c, \rho_c) = e^{-\beta \mathbf{p}_c^2/2m} \rho_c(\mathbf{q}_c). \tag{3.43}$$

By integrating the equations of motion with an appropriate scheme, such as a molecular dynamics integrator discussed previously or such as the symplectic and exact method discussed in Ceriotti *et al*[34], a pseudo-classical trajectory is obtained which can be used to compute centroid time correlation functions, which are effectively Kubo-transformed[35] time correlation functions

The idea was in essence that quasi-classical information can be extracted from the centroid mode of a wave-packet moving in a potential with a quantum mechanical correction to its trajectory *a la* Feynman and Hibbs, but that this correction could be generated by the exploration of local phase space by the beads of a PIMD simulation with a constrained centroid. In order to achieve this, the centroid of the ring-polymer would be treated as a (non-path-integral) molecular dynamics simulation on a potential field, only every time the potential was evaluated, a path integral simulation with fixed centroid would be run at that point in the MD run. The result would be an average force on the other normal modes, over the sub-simulation which would be used to correct the force obtained from the potential, and hence the dynamics.

Later, the concept was made more general in what is known as partially adiabatic centroid PIMD. The idea here is exactly the same; that the dynamics of the centroid are physically meaningful, in that the trajectory of the centroid represents a pseudo-classical path of the centre of mass of the delocalised particle density. Implementationally, though, PACMD is quite different. As the higher frequency normal modes are simply a ensemble phase space sampling device, altering their dynamics to sample more of phase space more quickly will not affect the dynamics of the centroid mode. The better the sampling of phase space, the more accurate the centroid trajectory will be. In PACMD, the masses of the non-centroid normal modes are artificially reduced by some arbitrary factor, so allowing them to move more quickly. This eliminates the two-step process to performing CPIMD; a single PIMD run can be performed with reduced (non-centroid) normal mode masses, which are reduced until convergence in desired observable is obtained. Performing molecular dynamics on such potentially light particles is, however, problematic due to error in the integration algorithm. It is usually necessary, then, to reduce the timestep as the centroid/non-centroid adiabaticity is turned up. The result is that the algorithm can be very expensive for light particles when the simulation must also have been converged with respect to the number of beads.

3.6.1 Normal Mode Transformations

The beads and springs, classical picture of the path integral discussed earlier is more than just an analogy, but a formal mapping which preserves all properties in a true isomorphism. It is then possible to invert the fundamental matrix of the system (of a ring polymer of beads connected by springs) as would be performed in classical mechanics to produce the monodromy matrix,

$$M = \begin{bmatrix} 2 & 1 & 0 & & -1 \\ 1 & 2 & 1 & & 0 \\ 0 & 1 & 2 & & 0 \\ & & & \ddots & \\ -1 & 0 & 0 & & 2 \end{bmatrix}^{-1} \tag{3.44}$$

and hence then transform the coordinate system into the normal-mode coordinates of the free ring polymer, by the relation:

$$\mathbf{u} = M\mathbf{q} \tag{3.45}$$

$$\mathbf{q} = M^{-1}\mathbf{u}, \tag{3.46}$$

where $\mathbf{u}$ is a vector of normal mode coordinates and $\mathbf{q}$ is a vector of coordinates in linear space.

This transformation is particularly relevant and important because the first normal mode of the system corresponds to the centre of mass, or centroid of the ring polymer, which is, of course exactly the variable which we hope to propagate in the CMD scheme.

Furthermore, for a closed ring polymer in free space, the monodromy matrix is in fact a Vandemonde matrix, and so the transformation can be viewed as a Fourier transform. As an operation which is performed very many times through the course of a simulation, this is a very important observation, as the symmetry of the linear transform can be readily exploited with a fast Fourier transform (FFT), which scales as $Nlog(N)$, rather than N^2.

$$q_k = \sum_{l=0}^{P-1} u_l e^{2\pi \mathbf{i} kl/P} \tag{3.47}$$

In the normal mode representation, the effective masses of the normal modes should be multiplied by the eigenvalues of 3.44. The complication of this is that if the Fourier approach is taken then linear combinations of eigenvalues are taken and every eigenvalue except the centroid and last mode should be

divided by $\sqrt{2}$ (on top of the usual FFT normalisation).

According to Marx [36], when in the normal-mode representation, it is possible to perform partially adiabatic CMD quickly and easily. Rather than operate the procedure in two parts as an MD propagation of the centroid and a centroid constrained propagation of the bead positions, the non-centroid normal modes can be accelerated by reducing their masses with respect to centroid mode (in the normal mode representation). A shorter timestep will be required to keep the integration of the faster dynamics stable, however once converged with respect to this "centroid adiabaticity parameter", γ, it is equivalent to the centroid moving on an effective potential generated by the other normal modes. This way of doing things is empirically much faster than the original way, at the expense of an arbitrary convergence parameter.

Therefore, the normal mode masses are multiplied by γ as:

$$M_I^{\prime s} = \gamma M_I, \quad s = 2, P, \tag{3.48}$$

where M_I is the atomic mass and s denotes the index of the normal modes.

3.7 Thermostatted CMD

In the past, PACMD calculations have been thermostatted in either of two ways; firstly a non-stochastic thermostat, with a deterministic effect, such as Nose-Hoover might be employed. Nose-Hoover thermostats are known to be non-ergodic in the long-time limit, however, so 'Nose-Hoover chains' were developed, though it (to my knowledge) has never been proven that this thermostat converges to ergodicity in the limit of the number of auxiliary chains.

The other approach is to perform a thermostatted, standard PIMD calculation of a long enough duration that N uncorrelated samples of the bead coordinates can be gathered. This set of positions and momenta will then sample from the Maxwell-Boltzmann distribution at the temperature of the thermostatted run and these samples can then be used to initialise N un-thermostatted (micro-canonical) PACMD runs. The resulting trajectories from these child calculations can be used to calculate N dynamical correlation functions which may be averaged to give a correlation function at the desired temperature.

In this work, the thermostat has been used in a different way. The objective was to model the friction in the ^3He spin-echo experiments, so having a model with a friction parameter is of particular importance. Rather than using the parameter to find the most efficient sampling, it would instead be used to find

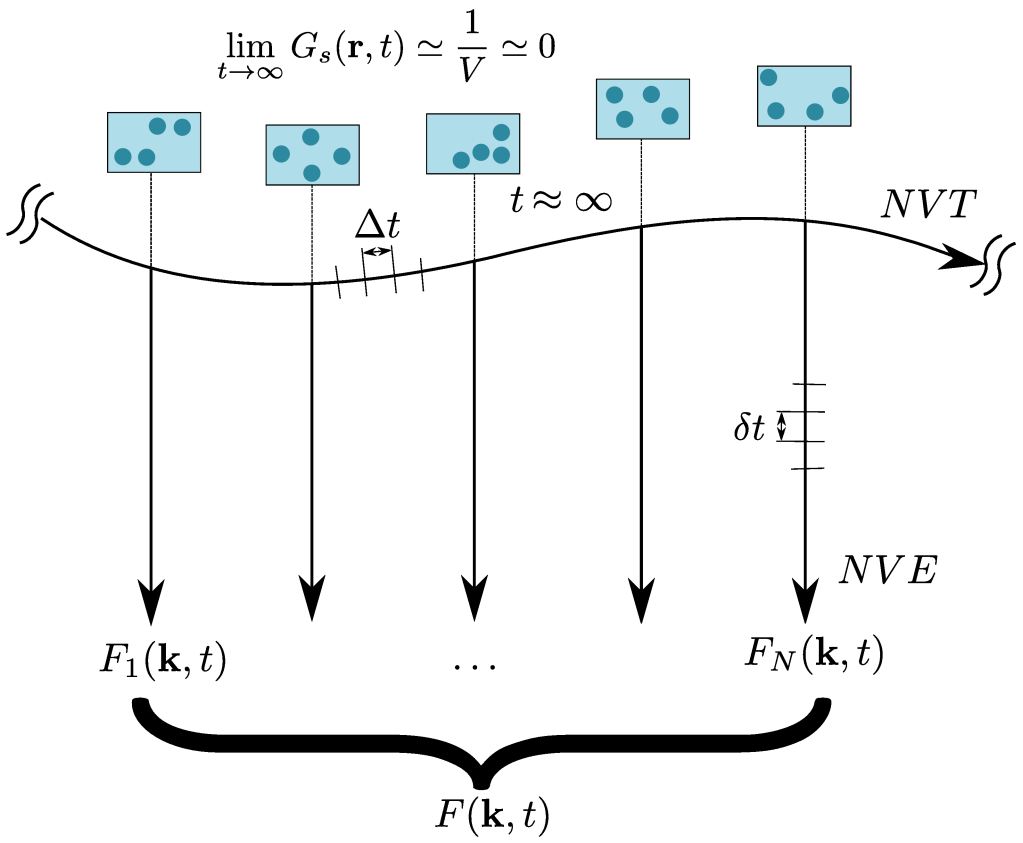

Figure 3.3: In past work [3], thermostatting has been applied to CMD by running a thermostatted (NVT) standard PIMD simulation and sampling it once some correlation function such as the self part of the Van-Hove function indicates that the system is uncorrelated with the past sample, at which point a microcanonical (NVE) simulation is spawned with the initial configuration of the parent at the point it was spawned. Measurements are taken of some observable on the child runs, and averaged over runs to give a result in a canonical ensemble. This approach was rejected for this work, for the reason it is usually employed, as we need to directly affect the dynamics of the system in order to see the effect of friction.

the value of friction which most closely matches the dynamics of the experiment. As it turns out, applying the simple, stochastic Langevin equation as an auxiliary equation of motion on the dynamics of the system can be made to ensure iso-thermal conditions. While this is a very effective thermostat [34][37], it is advantageous also because the Langevin equation has a term for viscous damping due to a friction with the heat-bath. This is represented by a scalar friction coefficient. This coefficient is what has been focussed on in the current work; in particular, how its choice affects the dynamics of the system through ISFs and then which choice most closely matches experiment through a fit with a set of ISFs at various momentum transfers.

The Langevin equation was originally intended as a recasting of Einstein's

Brownian motion in terms of momentum, and hence it includes not only a frictional damping term, but also a stochastic buffeting term which represents the random interactions of the particle as it moves through a sea of fictitious particles. Using the Langevin equation as a thermostat is possible because this second term can be made to counterbalance the effect of the damping, by judicious choice of coefficient to scale the magnitude of random noise.

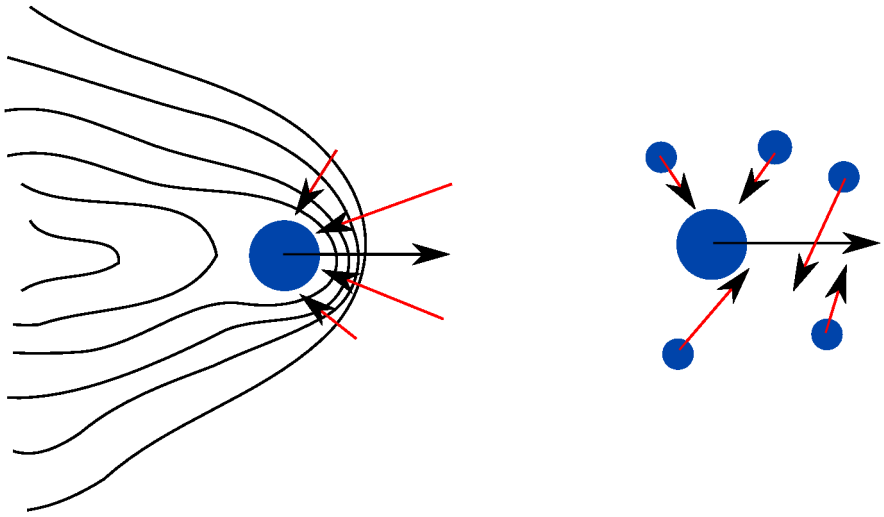

Figure 3.4: The effect of the Langevin thermostat is twofold, there is a frictional damping term as if the particle were moving through a viscous liquid and reversiblity brought in through the second stochastic term which represents a buffeting by a set of fictitious particles with random momentum.

In this capacity as thermostat, the Langevin equation is written,

$$\mathbf{F} \rightarrow \mathbf{F} - \gamma \mathbf{p} + \sqrt{\frac{2\gamma m}{\beta}}\xi(t), \tag{3.49}$$

where, as before $\mathbf{F}$ is the force acting on the particle, p is the corresponding momentum, m is its mass and β is thermodynamic β. γ is the friction coefficient, as seen in the first term representing the damping. $\xi(t)$ is a set of uncorrelated random numbers for every time, with zero mean and unit variance.

3.7.1 Thermostats in Other Coordinate Systems

It may be advantageous, rather than to thermostat the linear, internal coordinates of the bead-spring system, to apply the thermostat to the normal modes of the system. It has been shown [34] that the correlation times can be minimised for a harmonic oscillator potential by setting the friction parameters

for the Langevin equation on each of the normal modes to have the following analytic form:

$$\gamma_k = \begin{cases} 1/\tau_0, & k = 0 \\ 2\omega_k, & k > 0, \end{cases} \tag{3.50}$$

where τ_0 is the free parameter for thermostat correlation time, which is to be adjusted for fit with experiment.

In the normal mode representation, then, the path-integral Langevin thermostat equation on each atom, is written as

$$\mathbf{p_k} \rightarrow a_k \mathbf{p_k} + \sqrt{\frac{mP}{\beta}} b_k \xi_k, \tag{3.51}$$

where all quantities have their usual meanings and the friction parameters are applied to the normal modes, through a_k and b_k in the following way:

$$a_k = e^{-(\Delta t/2)\gamma_k} \tag{3.52}$$

$$b_k = \sqrt{1 - a_k^2} \tag{3.53}$$

The effect of this is to maximise the sampling of phase-space, under the assumption that the background potential is harmonic, while keeping the frictional damping on the centroid a free parameter. This was the scheme used in this work.

3.8 Correlation Functions from PIMD

In this work, the most important correlation function to consider was the ISF, as this is what was measured experimentally and so provides the means to compare directly with experiment. Starting from a general perspective however, we can start with a time-correlation function, as the ISF can be written in terms of an auto-correlation of Fourier coefficients of the density,

$$F(\mathbf{k}, t) = \langle \rho_{\mathbf{k}}(0) \rho_{\mathbf{k}}(t) \rangle, \tag{3.54}$$

where $\mathbf{k}$ is a particular wave-vector. This representation is particularly useful in this work, as the experiment measures ISFs along particular azimuths with a discrete set of momentum transfers, so for comparison with experiment, using this representation, ISFs with the same set of momentum transfers $\mathbf{k}$ could be generated from trajectory data. This is possible because we can write the

Fourier operator as:

$$\rho_{\mathbf{k}} = e^{i\mathbf{k}\cdot\mathbf{q}} \tag{3.55}$$

Performing the process in (3.54) is a $\mathcal{O}(N^2)$ operation, where N represents the number of sampled time-steps in this context. There exists a much faster way, in practice to calculate auto-correlation functions; the Wiener-Khinchin theorem states that the power spectrum of a process is the Fourier transform of its autocorrelation function. Using this knowledge, the auto-correlation can be written as:

$$A(\omega) = \int_{-\infty}^{\infty} \rho_{\mathbf{k}}(t) e^{2\pi \mathbf{i} t\omega}\, \mathrm{d}t \tag{3.56}$$

$$F(t) = \int_{-\infty}^{\infty} A(\omega) A(\omega)^* e^{-2\pi \mathbf{i} t\omega}\, \mathrm{d}\omega, \tag{3.57}$$

where the integrals are standard Fourier and inverse Fourier transforms and $*$ represents conjugation. This in itself does not gain anything in efficiency, but writing this expression discretely, we can apply the FFT, which scales as $\mathcal{O}(N\ln(N))$ and the computation is much more rapid.

Algorithm 2 Wiener-Khinchin ISF algorithm

Function $f : \mathbb{R}^n \to \mathbb{R}^n, \quad F \mapsto \langle \rho_{\mathbf{k}}(0)\rho_{\mathbf{k}}(t)\rangle$

$$\begin{aligned} A(\omega) &= FFT(\rho_{\mathbf{k}}(t)) \\ A(\omega) &\to A(\omega)A(\omega)^* \\ F(t) &= FFT(A(\omega)) \end{aligned} \tag{3.58}$$

End Function

3.8.1 Kubo Transform

CMD is based on the equations of motion which will generate a Kubo-transformed time- correlation function.[38] Exact quantum correlation functions must be

calculated through an inverse Kubo transform [31], which may be written as:

$$\bar{C}(\omega) = \frac{\hbar\beta\omega}{2}(coth(\frac{\hbar\beta\omega}{2}) + 1)\bar{C^*}(\omega), \tag{3.59}$$

where if C is the time correlation function of interest, then $\bar{C}$ is its Fourier transform and $\bar{C^*}$ is the Fourier transform of its Kubo transformed counterpart. The algorithm used to generate a time correlation function is given in algorithm 3. The function in (3.59) amounts to a smooth transition between a multiplation by unity for the "DC" mode up to a multiplication by a particular modes associated frequency in the limit of high frequency. This was implemented by working out firstly the corresponding frequency of the FFT coefficient, where the i^{th} is given by:

$$f_i = \left(\frac{i}{N * \delta t}\right)_{i=0}^{P}, \quad where: P = \begin{cases} N/2 - 1 & \text{if } N \text{ is even} \\ (N-1)/2 & \text{if } N \text{ is odd} \end{cases}, \tag{3.60}$$

in an FFT of dimension N, where δt is the sampling step.

Algorithm 3 Inverse Kubo Transform

Function $f : \mathbb{R}^n \to \mathbb{R}^n, \quad C \mapsto IKubo(C^*)$

$$\begin{aligned} \bar{C^*} &= FFT(C^*) \\ \bar{C} &= (\hbar\beta\omega/2) * (coth(\hbar\beta\omega/2) + 1)\bar{C^*}(\omega) \\ C &= IFFT(\bar{C}) \end{aligned}$$

End Function

3.8.2 Gaussian Approximation to ISF

Manolopoulos and Craig [39] strongly advocate generating ISFs from velocity autocorrelation functions via a "Gaussian approximation", due to the non-linearity of $e^{-\mathbf{k}\cdot\mathbf{q}}$. The Kubo-transform relations normally only hold for linear operators. Hence, taking the inverse Kubo-transform of the autocorrelation

of $e^{-\mathbf{k}\cdot\mathbf{q}}$ for trajectories generated using CMD breaks down for large values of momentum transfer.

The incoherent structure factor (the temporal Fourier transform of the self part of the Van- Hove function, as shown in eq(2.12)) can be approximated as

$$F_s(\mathbf{k},t) \approx e^{-\mathbf{k}^2\gamma(t)}, \tag{3.61}$$

where $\gamma(t)$ is the mean squared displacement of a particle in time t, given in terms of the velocity autocorrelation function by

$$\gamma(t) = -i\frac{\hbar t}{2m} + \frac{1}{3}\int_0^t dt'(t-t')C_{v\cdot v}(t'). \tag{3.62}$$

The velocity autocorrelation function is written in its usual form as

$$C_{v\cdot v}(t) = \frac{1}{N}\sum_{j=1}^{N}\langle \mathbf{v}_j(0)\cdot\mathbf{v}_j(t)\rangle \tag{3.63}$$

This approach was explored briefly, towards the end of this work, but concerns were raised about its use on this project. Since we want to extract exponential coefficients from the (Non-Gaussian profile) ISFs to show temperature dependent, quantum friction and extract the associated coefficients, whether this would indeed give suitable ISFs was questioned. Despite this, a version which takes this approach was written into the code and initial results look promising. It would be prudent for this to be tested more rigorously and ISFs compared and fitted with the biexponential model of decay in a subsequent project. Thanks to a very useful conversation with David Manolopoulos it arose that this could be the reason for discrepancies seen in some results for high momentum transfer (see chapter 4).

3.9 Potential Energy Surface

In order to perform a study of quantum dynamics, the background potential has to be considered. This could be calculated "on the fly", using an *ab-initio* DFT package, however the computational demands for such a procedure would be huge, and well beyond the scope of this project. In order to show temperature dependent friction, in the quantum regime, however, a much simpler form for the potential can be used. The system under study was strongly adiabatic with a factor of 100 between the mass of the Ruthenium atoms and Hydrogen adsorbate. For this reason, a rigid potential energy surface was constructed, with no dissipative terms. The rationale behind this was that all of

the dissipation will be mediated by the heat-bath.

Ruthenium has an HCP structure and the 0001 cleavage is hexagonal, with basis vectors,

$$\mathbf{a}_1 = a(1,0,0) \tag{3.64}$$

$$\mathbf{a}_2 = a(-\frac{1}{2}, \frac{\sqrt{3}}{2}, 0), \tag{3.65}$$

where a is the nearest-neighbour separation in the $11\bar{2}0$ direction. Using this as a basis, a simple sin-cos model was constructed of the potential energy surface (PES), with respect to the position of a Hydrogen atom, with the maximum on top of the Ruthenium atom, two non-degenerate minima and a bridge site, as a barrier mediating inter-site hopping. This arrangement was suggested by a sampling of the PES performed using CASTEP [40].

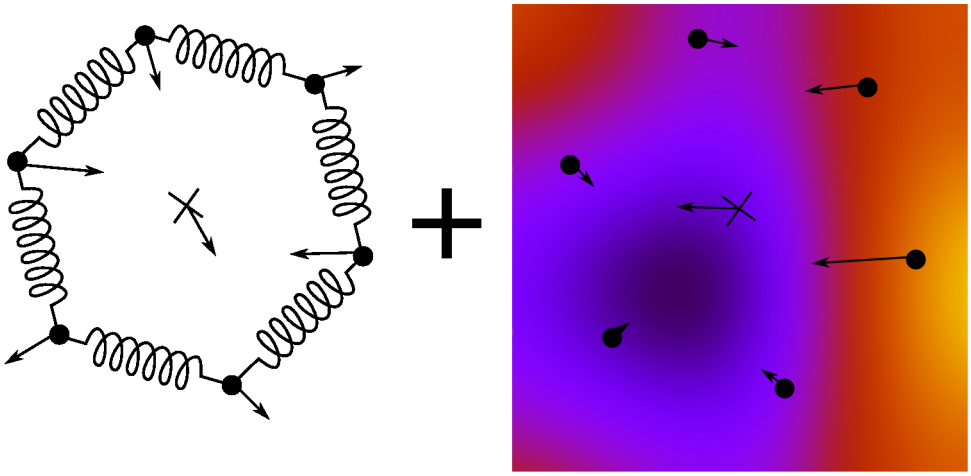

Figure 3.5: The forces when performing a PIMD calculation on a potential energy surface are obtained by separately finding the forces on each bead due to the internal, harmonic interactions of the bead-spring system and the forces on each bead due to the background potential energy surface ($-\nabla V$), and summing them.

3.9.1 CASTEP

CASTEP [40] is a widely used Density Functional Theory (DFT) code, which was used in this work for two reasons (a third, somewhat detached calculation is detailed in appendix B), firstly to roughly estimate the shape of the potential energy surface and secondly to provide well-converged values for the energy of the four sites in the sin-cos model for the PES, in order to parameterise it with realistic numbers.

To perform the grid sampling of energy surface, firstly lattice parameters were calculated using a primitive cell of bulk Ruthenium. This was converged with respect to plane-wave cut-off energy and Brillouin-zone sampling. A geometry optimisation was then performed.

To sample values from the PES, a cell was set up with 4 bi-layers of Ruthenium into the bulk, with the deepest layer constrained to bulk configuration. 10 Ångstroms of vacuum gap were initially placed in the z (perpendicular to plane) direction. It was found that the total-energy of the system held within 10meV after increasing the number of bilayers beyond 6 and the increasing the vacuum gap beyond 15 Ångstroms. The system was also geometry optimised in ionic positions (not cell vectors) in order to account for surface relaxations.

Once this 6 bi-layer, 15 Ångstrom vacuum-gap, 500eV plane-wave cut-off energy, 12x12x2 k-point system was prepared, the PES grid could be calculated on the irreducible wedge. In order to do this, a hydrogen was introduced, which was relaxed into the surface using a geometry optimisation (the only degree of freedom not constrained was the Hydrogen z-component). This would yield the energies of the PES. In practice, however, this turned out to be a very expensive operation for the number of points required, so the operation was rethought.

The geometry optimisation code in CASTEP does wavefunction extrapolation for each new step in configuration space, rather than initialising the wavefunction with random numbers. This can speed geometry optimisations up a great deal, and so whether this procedure could speed up the calculation of a PES was investigated. The rationale was that each step on the regular grid would only be a small perturbation to the wavefunction for reasonably dense samplings and hence should result in fewer iterations being necessary to converge the wavefunction.

This procedure was implemented simply by taking the loops over sampling grid into CASTEP rather than in a script calling CASTEP and calling the `geom_extrapolate` routine within them. The resulting speedup was useful, if not tremendous and this code will be released to users with a subsequent CASTEP release.

3.9.2 Interpolation

If a non-analytic, lattice-sampled form for the potential is used, then some consideration must be given to how the function varies between sampling points. Of course, in the limit of small sampling interval, the error tends to zero, but

in practice, the sampling of PES points is expensive, so the mesh is sampled at the minimum frequency at which observables are converged to some arbitrary tolerance and with respect to further sampling on an interpolated mesh.

The chosen interpolation method is important in that it should be continuous (unbroken) and smooth (has a convergent Taylor series). Two possibilities for this procedure are (bi/tri) cubic and Fourier interpolation.

3.9.2.1 Cubic-Spline Interpolation

If the function has known values on a regular grid, a third order polynomial,

$$f(x) = a + bx + cx^2 + dx^3, \tag{3.66}$$

can be fitted between grid points, preserving continuity by ensuring that the derivative of the fitting form,

$$\frac{df(x)}{dx} = b + 2cx + 3dx^2, \tag{3.67}$$

is constrained to be equal at nodes of the mesh. The coefficients, a, b, c and d can be solved for, if two points and two derivatives are known at the nodes bounding the relevant interval. If the points' coordinates are set to be 0 and 1, then it is trivial to work out the polynomial fitting coefficients, and as this amounts to solving a set of simultaneous equations, the problem can be written in matrix form as:

$$\mathbf{z} = \mathbf{A}\mathbf{y}, \tag{3.68}$$

where $\mathbf{z}$ is the vector of function values and derivatives bounding the unsampled region, $\mathbf{A}$ is the matrix associated with the linear equation and $\mathbf{x}$ is the vector of polynomial coefficients. In 1D, this can be written

$$\begin{bmatrix} f(0) \\ f(1) \\ f'(0) \\ f'(1) \end{bmatrix} = \begin{bmatrix} 2 & -2 & 1 & 1 \\ -3 & 3 & -2 & -1 \\ 0 & 0 & 1 & 0 \\ 1 & 0 & 0 & 0 \end{bmatrix} \begin{bmatrix} a \\ b \\ c \\ d \end{bmatrix}. \tag{3.69}$$

The matrix can then be analytically inverted by Gaussian elimination to give the vector of polynomial coefficients for the cubic interpolant on the interval:

$$\begin{bmatrix} a \\ b \\ c \\ d \end{bmatrix} = \begin{bmatrix} 0 & 0 & 0 & 1 \\ 1 & 1 & 1 & 1 \\ 0 & 0 & 1 & 0 \\ 3 & 2 & 1 & 0 \end{bmatrix} \begin{bmatrix} f(0) \\ f(1) \\ f'(0) \\ f'(1) \end{bmatrix}. \tag{3.70}$$

The same process can be applied in 2D and 3D, where the interpolation methods are known as bicubic and tricubic, respectively. In these cases attention must be paid to cross-derivatives and the matrix, **A** becomes 16x16 in 2D and 64x64 in 3D, if **z**, which represents the functional values and derivatives on the vertices of the N-D hyper-cube interval and **y** a correspondingly dimensioned object of fitting coefficients are represented as vectors in flattened form.

For the 3D case, in particular, this represents a large computational cost; the coefficients must be calculated for each interval on the sampled grid and the interpolated value calculated as:

$$E(\mathbf{x}) = \sum_{i=1}^{4} \sum_{j=1}^{4} \sum_{k=1}^{4} y_{ijk} x_1^{i-1} x_2^{j-1} x_3^{k-1}, \tag{3.71}$$

where E is the functional value as interpolated from the bounding grid-points on the interval, at $\mathbf{x}$ and y are elements from the 3D array of fitting coefficients when unflattened.

In practice, the coefficients are only calculated once per calculation and stored. The only expense then is to perform the operation in (3.71) whenever a functional value is required (or the equivalent in 2D).

3.9.2.2 Fourier Interpolation

An alternative to cubic interpolation is to use a Fourier interpolation, whereby all of the sampled data is used to sample each interpolated point rather than constructing a spline model. The method consists of taking a fast Fourier transform (FFT) of the sampled grid of functional values and then back transforming onto only the coordinates of interest, which cannot, unfortunately be done with a FFT.

This approach works well, but is expensive for dense grids, as a back-transform onto a single point in linear-space scales with the product of sampling points in every dimension. An alternative is to back-transform onto a much denser grid where a (tri/bi)linear or even nearest-neighbour interpolation would not

be detrimental to the accuracy of the calculations.

3.9.3 PES Model

As the point of the project was to show how atomic-scale friction can be temperature dependent through the inclusion of quantum effects, a model was sought that could be tuned readily (could be parameterised to give results for the experimental evidence which motivated the work) but was also general in the sense that this work should not be applicable only to one system, but should lead to a simple model for atomic-scale friction in general.

It should be made clear that this is not an approximation in order to gain accuracy but instead to improve the generality and transferability of the method for calculation of friction parameters to any system with non-degenerate, barrier mediated hopping sites. The method should still be good for hydrogen on ruthenium, as it amounts to a low order Fourier expansion of the ab-initio PES.

The symmetry of the ruthenium (0001) - hydrogen PES was preserved, by the construction of a Fourier series on the hcp(0001) basis vectors,

$$V(\mathbf{r}) = \sum_{i,n} A_n cos(n\mathbf{g}_i \cdot \mathbf{r}) + \sum_{i,m} B_m sin(m\mathbf{h}_i \cdot \mathbf{r}), \tag{3.72}$$

where the i indices run over a set of reciprocal lattice vectors (for basis, see figure 2.2, plus $\mathbf{b}_2$) and n and m run over the number of Fourier coefficients to include. For the simplest representation with all four important high-symmetry points, a set of reciprocal vectors:

$$\begin{aligned}
\mathbf{g}_1 &= \Gamma(1,0) \\
\mathbf{g}_2 &= \Gamma(cos(\frac{\pi}{3}), sin(\frac{\pi}{3})) \\
\mathbf{g}_3 &= \Gamma(-cos(\frac{\pi}{3}), sin(\frac{\pi}{3})) \\
\mathbf{h}_1 &= \mathbf{g}_1 \\
\mathbf{h}_2 &= -\mathbf{g}_2 \\
\mathbf{h}_3 &= \mathbf{g}_3,
\end{aligned} \tag{3.73}$$

where $\Gamma = 4\pi/(\sqrt{3}a)$. If two cos terms, $n = 1,2$ are included, this allows for distinct top and bridge sites, one sin term, $m = 1$ is included to give non-degenerate FCC and HCP sites. Then we have a PES which can be parameterised to have distinct top, bridge, FCC and HCP sites of the desired energy difference. See figure 3.6 for the form of the result.

In terms of accessing the sites and parameterising the model, the four high-

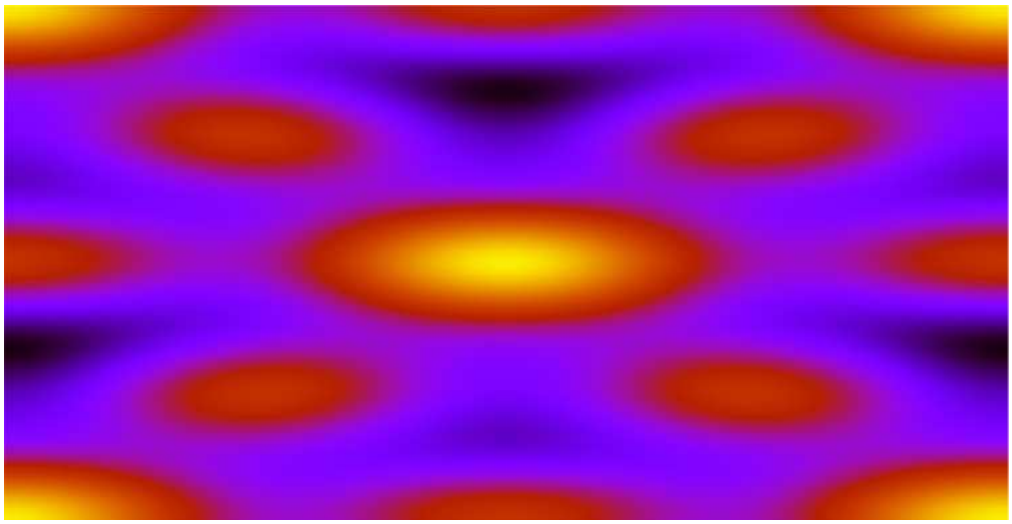

Figure 3.6: The trigonometric model for the potential energy surface has the same geometry as the ab-initio PES, together with each of the high symmetry points, including the top site (above a ruthenium atom), the bridge site (energy barrier) and two types of non-degenerate energy minima.

symmetry points can be written in terms of the Fourier coefficients as

$$\begin{aligned} V_{top} &= 3(A_1 + A_2) \\ V_{bridge} &= 3(A_2 - A_1) \\ V_{FCC} &= -\frac{3}{2}(A_1 + A_2 + \sqrt{3}B_1) \\ V_{HCP} &= -\frac{3}{2}(A_1 + A_2 - \sqrt{3}B_1) \end{aligned} \tag{3.74}$$

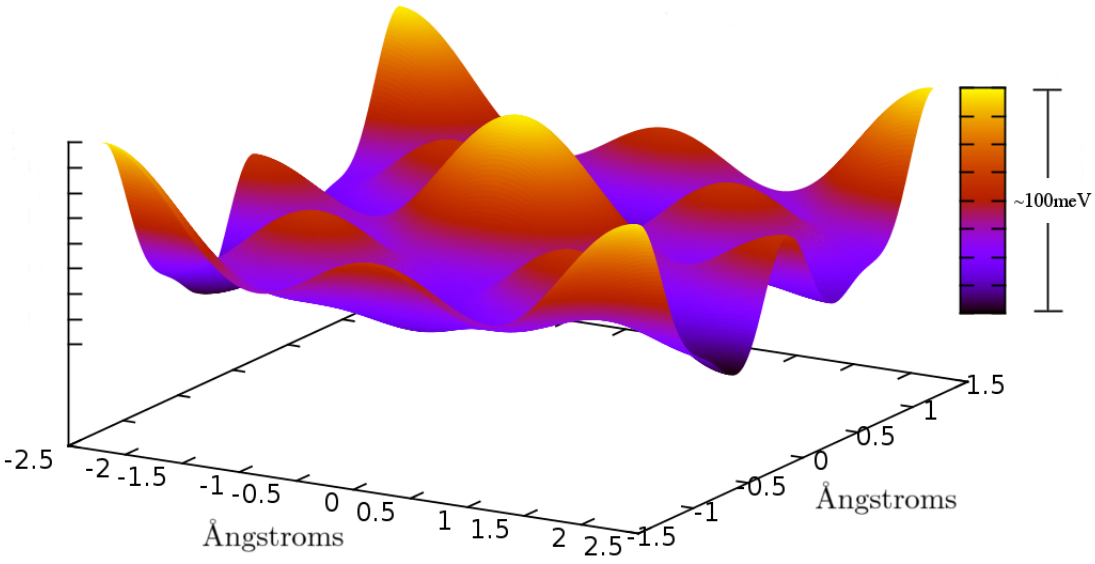

Figure 3.7: The potential energy surface, with spatial dimensions of the 2D PES denoted on the plane and the difference in energy between the various sites on the PES shown in the out of plane direction as both colour and height.

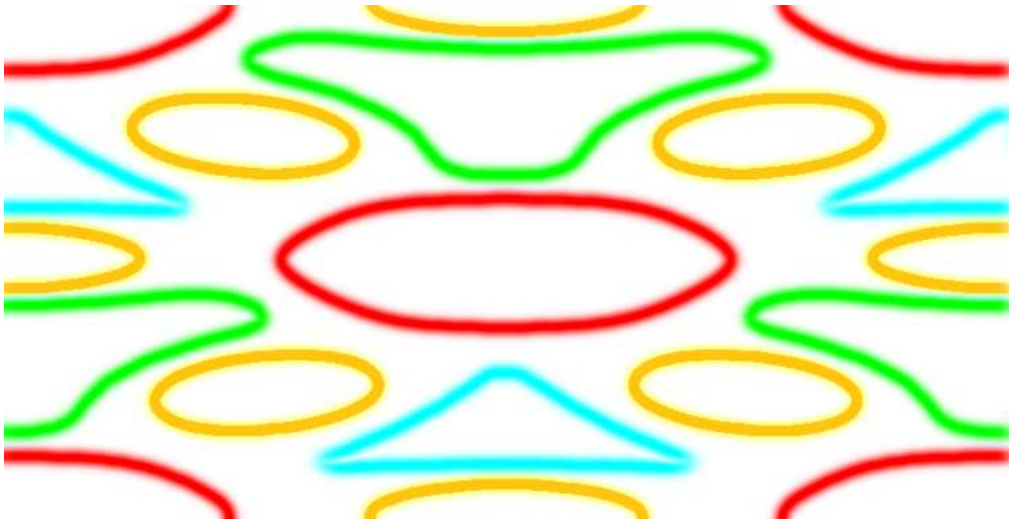

Figure 3.8: A schematic representation of the important sites on the potential energy surface. The top sites are represented by large, red ovals, the FCC sites by large, green, rounded triangles, the HCP sites by small, blue triangles and the bridge sites by small, yellow ovals. This picture was generated directly from the PES at a fixed, arbitrary energy contour, such that the sites are visibly distinct.

Chapter 4

Results

A CMD study of the behaviour of hydrogen adsorbates on a model of a ruthenium (0001) surface has been completed and compared directly with results from ^3He spin-echo interferometry. The experiment was carried out with 0.22ML hydrogen on the surface, so a 2x2 supercell of the PES discussed in chapter 3 has been used with a single hydrogen occupation which gives a quarter monolayer coverage in the simulation.

The centroid adiabaticity parameter and timestep were tuned carefully in order to give good, well converged results; an adiabaticity of 0.0025 and a timestep of 0.25fs were chosen after extensive trials.

While the method can give ISF data down to lower correlation times than the experiment, it is unimportant both because there is no experimental data to compare it with and because it is thought that phonon modes become an important factor in the shape of the ISF at such small correlation times. As the PES has no dissipation term, phonons will not be observed on the simulated substrate and only transverse-modes of the adsorbate will be seen. This presents itself as a Gaussian form, which represents ballistic motion in the ISF. As all motion can be viewed as ballistic on very short length scales, all in all, this initial part of the ISF does not hold much useful information. The simulated ISFs are then presented on the same scale as experiment.

Part of the interest of approaching the problem with a molecular dynamics technique was that it would be possible to see the trajectories of the adsorbate, something which is not possible with experiment. While there is a one to many mapping from ISFs to trajectories, a trajectory can certainly be produced which presents the correct behaviour, if not identically the trajectory of the actual adsorbate in reality. A set of simulated trajectories for comparison of temperature and classical versus quantum diffusion is presented in figure 4.1.

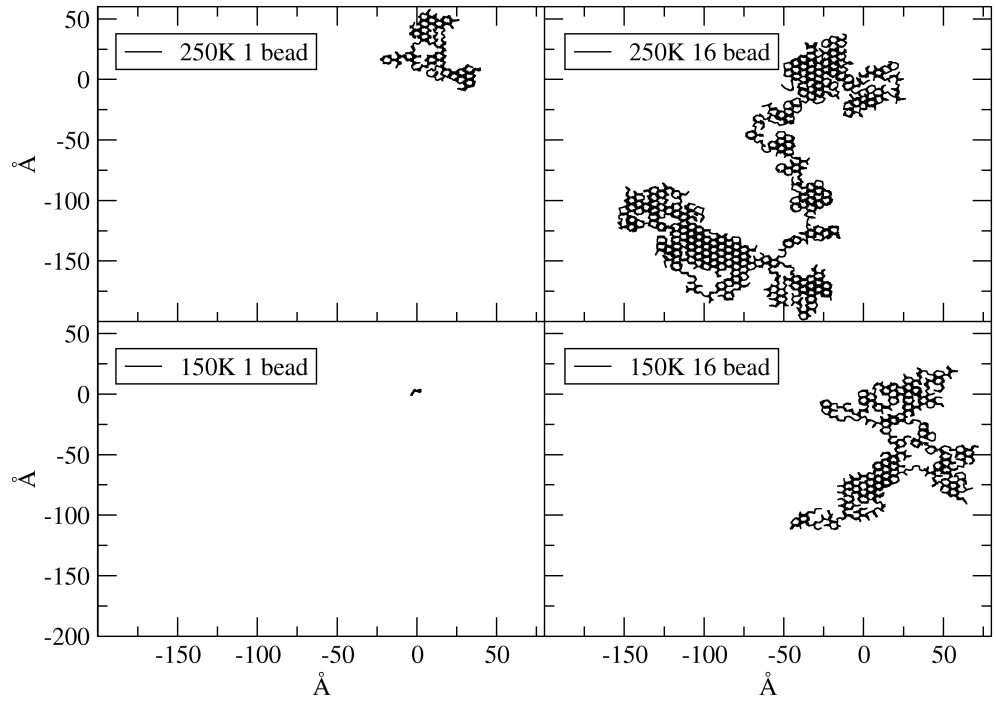

Figure 4.1: Four trajectories are explored in order to show the differences in adsorbate behaviour between the classical (1 bead) dynamics on the left and the quantum mechanical (16 bead) behaviour on the right. Also the two experimentally measured temperatures are shown, 250K and 150K. It is clear that 250K diffuses further than 150K, and the quantum mechanically correct behaviour increases the diffusion, not only for 150K, but is also an important effect at 250K. All trajectories run for 12.5ns and the friction parameter was set at $\eta = 0.01ps^1$.

What is immediately striking is that quantum behaviour effects the dynamics of diffusion not only at 150K, but is strongly apparent also at 250K. Care must be taken not to draw too much from single trajectories, as the behaviour presented may be an outlier, however, this was seen to be the case in most of the data that has been generated and examined; quantum effects play a role even at 250K in the mechanism of diffusion.

While trajectories are useful for visual inspection of the dynamics of the adsorbate, for comparison with experiment ISFs are necessary. Principally ISFs were the main observable against which the PIMD was converged with respect to number of beads. It can be seen in figure 4.2 that ISFs are visually converged after about 16 beads. In that example, calculated for the trajectories above, more evidence can be seen for the change in diffusive behavior from 150K to

250K and the necessity for quantum dynamics.

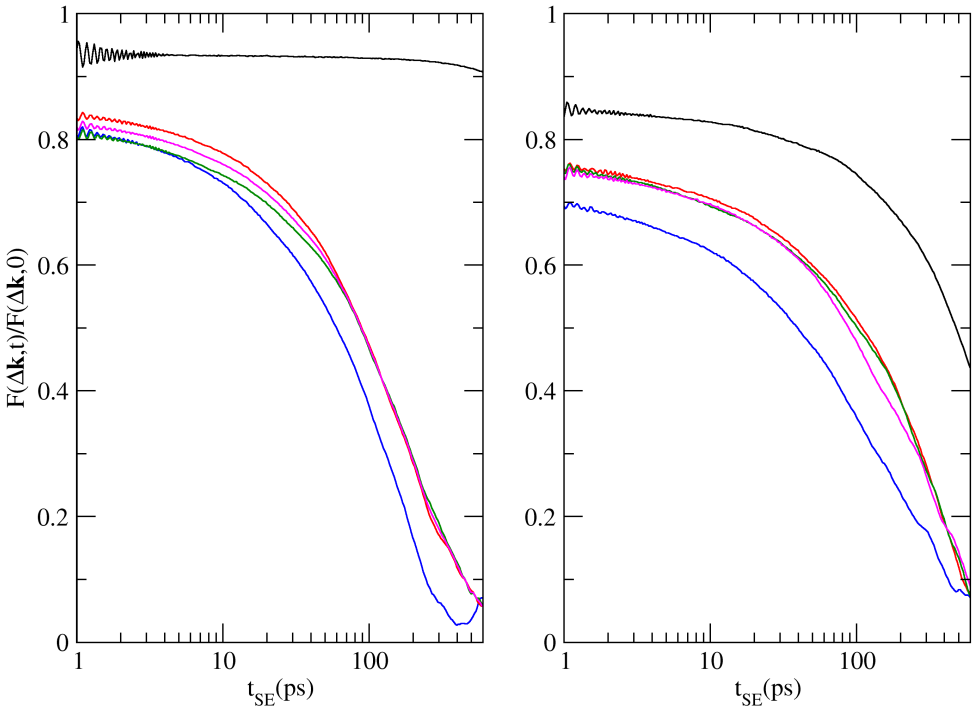

Figure 4.2: A convergence graph of the ISFs is presented. The ISFs are plotted with a time-window of 1 to 600 ps for consistency with the presentation of experimental data.The figure shows 150K on the left and 250K on the right. It is clear that the 150K 1-bead (classical) case exhibits very little diffusion, while at 250K there is a decay. As for the quantum convergence, the calculations with 4 (blue), 8 (red), 16 (green) and 32 (pink) beads are shown. It is clear that they show more decay than the classical case and that there is a convergence towards a particular profile. This data was generated along the $\langle 11\bar{2}0 \rangle$ azimuth with a momentum transfer magnitude of $1\mathring{A}^{-}1$ at a friction of $\eta = 0.01ps^{-1}$, and averaged over a consistent number of trajectories.

As this data is averaged over many trajectories, the behaviour presented is more compelling than that of the single trajectories picture. It can clearly be seen that at 150K, the change in profile and hence increase in diffusion events from classical to fully converged quantum mechanical dynamics is immense. The adsorbate is almost diffusionless, classically, at 150K. It is perhaps the 250K picture which is the more interesting result however, as quantum effects rarely contribute so strongly to phenomena so close to room temperature, but are necessary in order to fully characterise the decays in the ISF.

Fitting the two exponential model to the data turned out to be an extremely awkward, unstable and time consuming challenge. This was in part due to the

very different time-scales on which the diffusion processes occur (part of the reason why the ISFs have been plotted with logarithmic time scales is to show this), leading to a very ill-conditioned problem, but also because the functional space has local minima and undefined regions, when trying to fit with a numerical optimiser (a standard Levenberg-Marquart minimiser). After a lot of effort, a rough estimate for the α could be determined, but not well enough to be confident in the results.

The Cambridge surface physics group has, however, developed a Bayesian fitting system for fitting the model against experimental data. While much more computationally demanding, the stability of this method is much better, so all further fit were performed using this system. Data fitted with the LM minimiser was still used however to be sure that the simulation was not giving wildly different answers at increasing bead numbers, see 4.3.

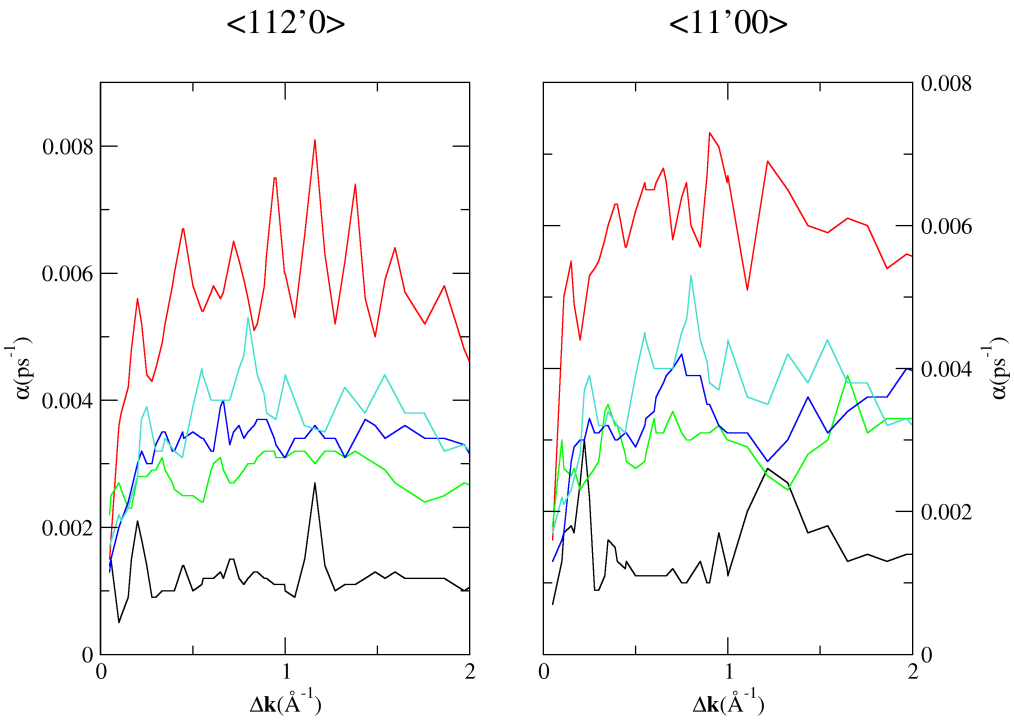

Figure 4.3: The $\alpha(\Delta\mathbf{k})$ was also checked for convergence with respect to the number of beads in the calculation. Shown here is convergence data for both principle azimuths at a friction coefficient $\eta = 0.01ps$ for 1 bead (black), 4 beads (red), 8 beads (green), 16 beads (blue), 32 beads (turquoise).

Of course with the amount of noise in these fits it is impossible to tell how well the $\alpha(\Delta\mathbf{k})$ plots are converged with bead number, though they show markedly similar behaviour in the same region, plus the ISFs were all checked to be well converged above 16 beads.

The next step was to attempt to fit friction values to experiment by running well converged simulations at a series of friction values to calculate several $\alpha(\Delta\mathbf{k})$ plots to compare with experiment. This was completed at 250K (figure 4.4) and 150K (figure 4.5), along both azimuths.

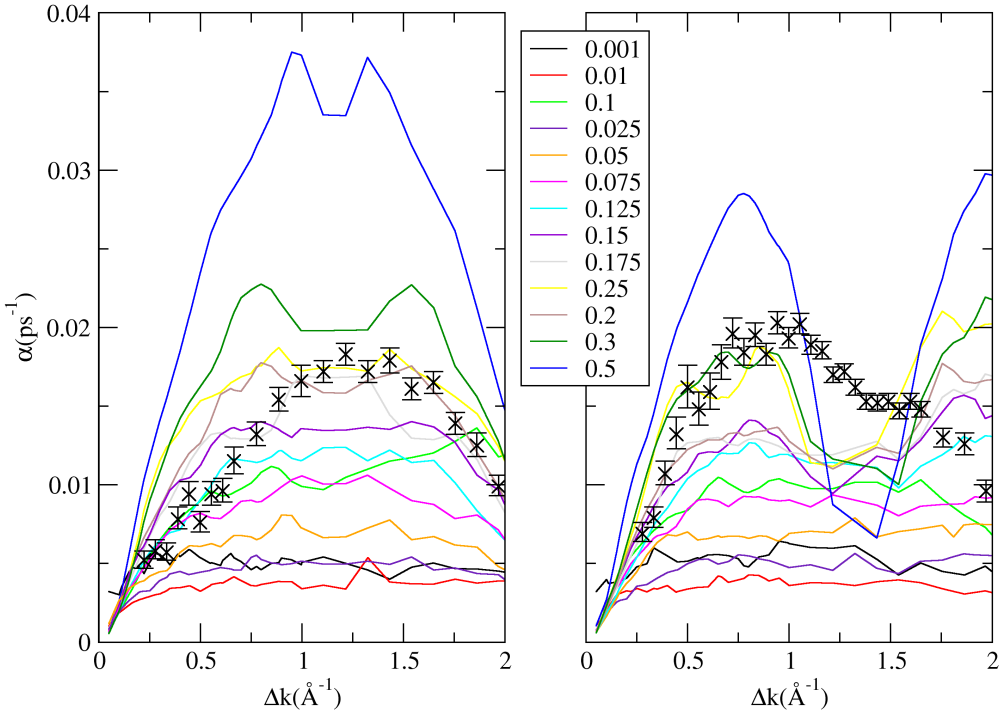

Figure 4.4: Simulated $\alpha(\Delta\mathbf{k})$ plots have been calculated at 13 values of friction in $\AA^{-1}$ at 250K along both the $\langle 1\bar{1}00\rangle$ azimuth on the left and the $\langle 11\bar{2}0\rangle$ azimuth on the right. All calculations were completed with 32 beads and plotted against experimental data (black crosses). It is clear that there is not a good agreement between the mechanism of diffusion presented by the simulation and experiment beyond about $1\AA^{-1}$ of momentum transfer, however, in the low momentum transfer limit, it is clear that before the effect of interactions becomes apparent the agreement between simulation and experiment is quite good.

The data does not match over the entire domain, however this is to be expected, as we have investigated a very simplified model for the potential energy surface with no inter-adsorbate interactions. It is suspected that effect of such interactions will be to correct for the profile of the curves in the limit of large momentum transfer, as has been witnessed in the Monte-Carlo simulations performed by the Cambridge surface physics group before this project. Alternatively, as discussed in chapter 3 the effect could be due to the nonlinearity of the exponential operator in the generation of ISFs.

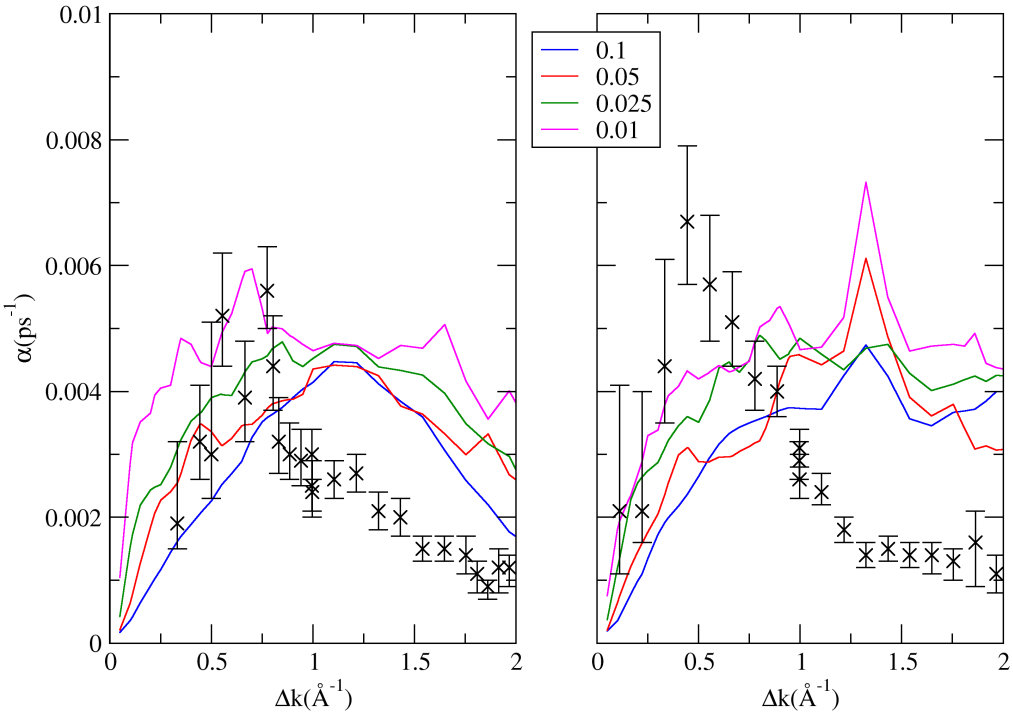

Figure 4.5: Again, simulated $\alpha(\Delta\mathbf{k})$ plots have been calculated at various values of friction in $\mathring{A}^{-1}$, but this time at 150K along both the $\langle 1\bar{1}00\rangle$ azimuth on the left and the $\langle 11\bar{2}0\rangle$ azimuth on the right. All calculations were completed with 32 beads and plotted against experimental data (black crosses). In the 150K case, it is more difficult to map between the simulated data and the experimental data, as there are fewer experimental data-points. For clarity, then, four simulated plots which appear to bracket the experimental data in the low momentum transfer regime.

What is striking about the results is that they do match the low momentum transfer regions of both azimuths at both temperatures and give different best-fit friction parameters at each temperature. At 250K the friction parameter η lies somewhere between about 0.125 and 0.2 $\mathring{A}^{-1}$ whereas at 150K, while it is much more difficult to tell, because of the sparsity of the data in the low momentum transfer regime, across both azimuths, the friction parameter η is likely to be $< 0.05\mathring{A}^{-1}$.

The result of this, is that even though the curves have not been matched exactly, there has still been shown to be a significant difference in the best-fit friction parameters for a system at two different temperature.

Chapter 5

Conclusions

It has been shown that there is a clear, quantum-mechanical basis for friction. In the results presented in chapter 4 it was seen that centroid molecular dynamics together with a Langevin thermostat was used to generate ISFs for comparison with experiment. The first result was that there was no value of frictional damping for which the ISFs generated from classical MD trajectories were qualitatively similar in profile to experimental ISFs. In the limit of large numbers of beads, however, in the case of CMD, the ISFs converge to self-consistency, but also tend toward closer agreement with experiment.

The second, more compelling evidence for the technique is given by $\alpha - \Delta k$ plots, generated by fitting a bi-exponential model to both experimental and simulated ISFs at every experimentally sampled momentum transfer, at various values of frictional damping. The profile of the experimental curves could be matched, with particular values of friction in the low momentum-transfer regime.

What is profoundly interesting about the fits, however, is that we see temperature dependent friction; that is, a single frictional damping parameter cannot be used to best-fit both the data at 150 and 250 Kelvin. This was the hypothesis of the collaborating experimental group and modelling it was the aim of this project.

Two possible explanations for the disparity in the profile of the $\alpha - \Delta k$ curves along the $(11\bar{2})$ azimuth have been mooted. Firstly, that Hydrogen-Hydrogen interactions are the cause. In previous work, the Cambridge surface physics group [Eliza] has performed quantum Monte-Carlo calculations with and without a dipole-dipole term in the potential. This has been seen to correct for the difference in profile between the experimental and simulated $\alpha - \Delta k$ curves as Δk increases. The other possibility is that, as discussed by Craig and Manolopoulos[41], the non-linearity of the density operators in the Kubo-transform is to blame for

this phenomenon.

The groundwork for investigating this has now been laid; the software package which was used to perform the calculations has recently been updated in order to explore the observed deviations. Inter-particle potentials as well as generating ISFs from the velocity autocorrelation, through the Gaussian approximation are now supported. So, it should be straightforward to show in a subsequent project that either or both of these options will improve the results in the high momentum transfer, $(11\bar{2})$ azimuth regime.

These disparities do not take away from the overall finding, however, that is CMD, together with a stochastic, Langevin thermostat and a simple model for the potential energy surface have been used to give a quantum mechanical basis for temperature dependent friction, as seen experimentally for hydrogen on a ruthenium surface and that quantum mechanical effects are important even at the relatively high temperature of 250K.

5.1 Further Work

The Cambridge surface physics group has also measured that when deuterium is used as the adsorbate, the interstitial hopping rate diminishes greatly beyond what is expected. They have also developed a large set of data for H and D adsorbates on nickel, for which the methods outlined in this work could be applied.

5.2 Evaluation

Apart from a slow start, mostly thanks to computational and programmatic difficulties, together with many tangents and fruitless side-projects (see appendices), this project has been broadly successful, in my view. We have shown what we set out to show and we have matched experiment with good agreement in at least the domain of low momentum transfer. Furthermore, the technique gives more insight into the phenomena than alternatives such as QMC. I think that more is still to come; I have some confidence that the issues with the high momentum transfer regime will be settled and that the technique will continue to show its efficacy for other systems. That, however, is for someone else, in a subsequent project to address.

Appendix A

Generalised Langevin Equation Thermostat

It has been shown recently[34] that through the use of the generalised Langevin equation (GLE), better efficiency of phase-space sampling can be obtained with repect to Langevin equation thermostats. It was initially hoped that through the use of a generalised Langevin thermostat, more information about the friction could be generated in this project.

The GLE approach is formulated by writing the coefficients in the damping and stochastic terms in (3.49) as matrices,

$$\mathbf{F}' \rightarrow \mathbf{F}' - \Gamma_1 \mathbf{p}' + \sqrt{\frac{\mathbf{M}}{\beta}} \Gamma_2 \xi, \tag{A.1}$$

where,

$$\Gamma_1 = e^{-(\Delta t/2)\gamma^T}, \tag{A.2}$$

and,

$$\Gamma_2^T \Gamma_2 = \Gamma_1 C + C \Gamma_1^T, \tag{A.3}$$

where Γ_1 and Γ_2 are called the drift and diffusion matrices, respectively and C is the static covariance matrix. The primed vectors represent the forces and momenta of each degree of freedom, of each bead of each atom augmented with s auxiliary variables, such that taking an individual DoF, bead and atom, what was before a scalar becomes a vector;

$$\mathbf{p}'^{\alpha}_{i,j} = \begin{bmatrix} p^{\alpha}_{i,j} \\ \mathbf{s}^{\alpha}_{i,j\cdot} \end{bmatrix} \tag{A.4}$$

Unfortunately, since the fitting was so unreliable and noisy, it was hard to ex-

tract frictional damping parameters even with Langevin thermostats, and because the relationship between a GLE drift matrix and the physical friction was unclear, this approach was abandoned.

The method was, however, implemented and a version of the procedure described in Ceriotti *et al* [42] for generating matrices was implemented. The approach was not of particular note, except that a different approach to generating correlation times for the optimiser was used.

Ceriotti describes a fitting procedure, whereby GLE matrices can be generated with various properties. In this work, we were most concerned with the canonical case. A GLE matrix is produced which gives more efficient thermostatting over a wide range in frequency, versus a Langevin thermostat, when applied to a harmonic oscillator. This work will not discuss the importance of the harmonic oscillator, except to say that it is an important local limit of smooth, continuous systems such as have been studied.

Firstly, autocorrelation times of potential and total energy can be defined as,

$$\tau_V = \frac{1}{\langle V^2 \rangle} \int_0^\infty \langle (V(t) - \langle V \rangle)(V(0) - \langle V \rangle) \rangle dt, \tag{A.5}$$

$$\tau_H = \frac{1}{\langle H^2 \rangle} \int_0^\infty \langle (H(t) - \langle H \rangle)(H(0) - \langle H \rangle) \rangle dt. \tag{A.6}$$

Ceriotti goes on to define a renormalised coupling efficiency:

$$\kappa(\omega) = (\tau(\omega)\omega)^{-1}, \tag{A.7}$$

which allows for the definition of a merit function such as

$$\chi = (\sum_i |log(\kappa(\omega_i))|^m)^{1/m}, \tag{A.8}$$

where m defines the order of the norm and ω_i are on a logarithmic grid in the fitting range, for a canonical thermostat. This approach allows the use of generic non-linear optimisation procedures, such as l-BFGS or Levenberg-Marquardt, which were both used in this work.

The crux of this method, then is in producing τ values from the GLE matrices. If,

$$\tau_{ijkl} = \int_0^\infty (x_i(t)x_j(t)x_k(0)x_l(0) - \langle x_i x_j \rangle \langle x_k x_l \rangle) dt \tag{A.9}$$

Ceriotti writes that this can be done through spectral decomposition, by writ-

ing:

$$X_{ijkl} = \sum_{mn} \frac{O_{im}(O^{-1}C)_{ml}O_{jn}(O^{-1}C)_{nk}}{\alpha_m + \alpha_n}, \tag{A.10}$$

where O is the matrix of eigenvectors of Γ_1 and α the corresponding eigenvalues. Likewise, C can be computed from (A.3) in a similar way by,

$$C_{ij} = \sum_{kl} \frac{O_{ik}(O^{-1}\Gamma_2\Gamma_2^T O^{-T})_{kl}O_{jl}}{\alpha_k + \alpha_l}, \tag{A.11}$$

then

$$\tau_{ijkl} = \frac{1}{4}(X_{ijkl} + X_{ijlk} + X_{klij} + X_{lkij}), \tag{A.12}$$

and

$$\tau_H = \frac{\omega^4\tau_{qqqq} + 2\omega^2\tau_{qqpp} + \tau_{pppp}}{\omega^4 c_{qq}^2 + 2\omega^2 c_{qp}^2 + c_{pp}^2}, \quad \tau_V = \frac{\tau_{qqqq}}{c_{qq}^2}. \tag{A.13}$$

This is claimed to be a more efficient way of computing C from (A.3), and generating τ values, than the "direct" approach.

In this work, however, another approach was taken. Firstly in computing C, (A.3) is a continuous Lyapunov equation. The direct approach is presumably to take

$$(I \otimes \Gamma_1 + \Gamma_1^T \otimes I)\,\mathrm{vec}(C) = \mathrm{vec}(\Gamma_2\Gamma_2^T), \tag{A.14}$$

where $\otimes$ is the Kronecker product and *vec* represents the "flattening" of a matrix into a vector, so that C can be solved for easily. Since the matrix in parentheses, multiplying $vec(C)$ is N^4, this is an extremely expensive operation. The solution can be computed in $O(N^3)$ operations, however, by QR factorisation and simultaneous back-substitution [43].

Since the integrand of (A.9) may be written as,

$$x_i(t)x_j(t)x_k(0)x_l(0) - \langle x_i x_j\rangle\langle x_k x_l\rangle = (e^{-|t|\Gamma_1}C)_{ik}(e^{-|t|\Gamma_1}C)_{jl} + (e^{-|t|\Gamma_1}C)_{il}(e^{-|t|\Gamma_1}C)_{jk}, \tag{A.15}$$

it was recognised that quantities such as $(e^{-|t|\Gamma_1}C)_{ik}(e^{-|t|\Gamma_1}C)_{jl}$ are tensor products of permuted matrices, and so:

$$(e^{-|t|\Gamma_1}C) \otimes (e^{-|t|\Gamma_1}C) = (e^{-|t|\Gamma_1} \otimes e^{-|t|\Gamma_1})(C \otimes C), \tag{A.16}$$

which may be written as

$$(e^{-|t|\Gamma_1} \otimes e^{-|t|\Gamma_1})(C \otimes C) = (e^{-t(\Gamma_1 \oplus \Gamma_1)})(C \otimes C), \tag{A.17}$$

if we are only concerned with the positive part of the integral in (A.9) and

where $\oplus$ represents the Kronecker sum. Integrating from 0 to ∞, then,

$$\int_0^\infty (e^{-t(\Gamma_1 \oplus \Gamma_1)})(C \otimes C)dt = (\Gamma_1 \oplus \Gamma_1)^{-1}(C \otimes C). \tag{A.18}$$

If we expand out the Kronecker sum, then,

$$(\Gamma_1 \otimes I + I \otimes \Gamma_1)X = C \otimes C, \tag{A.19}$$

which can be written as a Lyapunov equation, which can be solved in the same way as above! The elements can be summed, following this procedure to give values of τ.

References

[1] A. Jardine, H. Hedgeland, G. Alexandrowicz, W. Allison, and J. Ellis, "Helium-3 spin-echo: Principles and application to dynamics at surfaces," *Progress in Surface Science*, vol. 84, no. 1112, pp. 323 – 379, 2009.

[2] A. P. Jardine, G. Alexandrowicz, H. Hedgeland, W. Allison, and J. Ellis, "Studying the microscopic nature of diffusion with helium-3 spin-echo," *Phys. Chem. Chem. Phys.*, vol. 11, pp. 3355–3374, 2009.

[3] D. Marx and J. Hutter, *Ab Initio Molecular Dynamics: Basic Theory and Advanced Methods*. Ab Initio Molecular Dynamics: Basic Theory and Advanced Methods, Cambridge University Press, 2009.

[4] J. Strömquist, L. Bengtsson, M. Persson, and B. Hammer, "The dynamics of h absorption in and adsorption on cu(111)," *Surface Science*, vol. 397, no. 13, pp. 382 – 394, 1998.

[5] C. Mak, C. Daly, and J. Krim, "Atomic-scale friction measurements on silver and chemisorbed oxygen surfaces," *Thin Solid Films*, vol. 253, no. 12, pp. 190 – 193, 1994.

[6] B. N. J. Persson and A. I. Volokitin, "Electronic friction of physisorbed molecules," *The Journal of Chemical Physics*, vol. 103, no. 19, pp. 8679–8683, 1995.

[7] R. J. Cannara, M. J. Brukman, K. Cimatu, A. V. Sumant, S. Baldelli, and R. W. Carpick, "Nanoscale friction varied by isotopic shifting of surface vibrational frequencies," *Science*, vol. 318, no. 5851, pp. 780–783, 2007.

[8] G. J. Germann, S. R. Cohen, G. Neubauer, G. M. McClelland, H. Seki, and D. Coulman, "Atomic scale friction of a diamond tip on diamond (100) and (111) surfaces," *Journal of Applied Physics*, vol. 73, no. 1, pp. 163–167, 1993.

[9] M. Hirano, "Atomistics of friction," *Surface Science Reports*, vol. 60, no. 8, pp. 159 – 201, 2006.

[10] J. Krim, "Surface science and the atomic-scale origins of friction: what once was old is new again," *Surface Science*, vol. 500, no. 1, pp. 741–758, 2002.

[11] P. Egelstaff, *An Introduction to the Liquid State*. Oxford Series on Neutron Scattering in Condensed Matter, Clarendon Press, 1994.

[12] C. Kittel, *Introduction to Solid State Physics*. Wiley, 2004.

[13] D. M. Eigler and E. K. Schweizer, "Positioning single atoms with a scanning tunnelling microscope," *Nature*, vol. 344, no. 6266, pp. 524–526, 1990.

[14] J. Ellis, K. Hermann, F. Hofmann, and J. P. Toennies, "Experimental determination of the turning point of thermal energy helium atoms above a cu(001) surface," *Phys. Rev. Lett.*, vol. 75, pp. 886–889, Jul 1995.

[15] J. Ellis, A. P. Graham, and J. P. Toennies, "Quasielastic helium atom scattering from a two-dimensional gas of xe atoms on pt(111)," *Phys. Rev. Lett.*, vol. 82, pp. 5072–5075, Jun 1999.

[16] E. Pike and P. Sabatier, *Scattering, Two-Volume Set: Scattering and inverse scattering in Pure and Applied Science*. Elsevier Science, 2001.

[17] U. Heiz and U. Landman, *Nanocatalysis*. NanoScience and Technology, Springer, 2007.

[18] T. Brückel, G. Heger, D. Richter, and R. Zorn, *Neutron Scattering (A Series of Lecture Notes)*. Schriften des Forschungszentrums Jülich, Forschungszentrum Jülich, Zentralbibliothek, 2007.

[19] C. T. Chudley and R. J. Elliott, "Neutron scattering from a liquid on a jump diffusion model," *Proceedings of the Physical Society*, vol. 77, no. 2, p. 353, 1961.

[20] E. M. McIntosh, K. T. Wikfeldt, J. Ellis, A. Michaelides, and W. Allison, "Quantum effects in the diffusion of hydrogen on ru(0001)," *The Journal of Physical Chemistry Letters*, vol. 4, no. 9, pp. 1565–1569, 2013.

[21] D. Rapaport, *The Art of Molecular Dynamics Simulation*. Cambridge University Press, 2004.

[22] L. Landau and E. Lifshits, *Mechanics 1*. Butterworth Heinemann, Elsevier Butterworth-Heinemann, 1976.

[23] R. Feynman, A. Hibbs, and D. Styer, *Quantum Mechanics and Path Integrals*. Dover books on physics, Dover Publications, Incorporated, 2010.

[24] D. Derbes, "Feynman's derivation of the schrödinger equation," *American Journal of Physics*, vol. 64, no. 7, pp. 881–884, 1996.

[25] U. Mosel, *Path Integrals in Field Theory: An Introduction*. Advanced Texts in Physics, Springer Verlag, 2004.

[26] M. Tuckerman, *Statistical Mechanics and Molecular Simulations*. Oxford Graduate Texts, Oxford University Press, UK, 2008.

[27] D. Chandler and P. G. Wolynes, "Exploiting the isomorphism between quantum theory and classical statistical mechanics of polyatomic fluids," *The Journal of Chemical Physics*, vol. 74, no. 7, pp. 4078–4095, 1981.

[28] B. J. Berne and D. Thirumalai, "On the simulation of quantum systems: path integral methods," *Annual Review of Physical Chemistry*, vol. 37, no. 1, pp. 401–424, 1986.

[29] N. Blinov and P.-N. Roy, "Operator formulation of centroid dynamics for bose–einstein and fermi–dirac statistics," *The Journal of Chemical Physics*, vol. 115, no. 17, pp. 7822–7831, 2001.

[30] R. P. Feynman and H. Kleinert, "Effective classical partition functions," *Phys. Rev. A*, vol. 34, pp. 5080–5084, Dec 1986.

[31] J. Cao and G. A. Voth, "The formulation of quantum statistical mechanics based on the feynman path centroid density. i. equilibrium properties," *The Journal of Chemical Physics*, vol. 100, no. 7, pp. 5093–5105, 1994.

[32] E. A. Polyakov, A. P. Lyubartsev, and P. N. Vorontsov-Velyaminov, "Centroid molecular dynamics: Comparison with exact results for model systems," *The Journal of Chemical Physics*, vol. 133, no. 19, p. 194103, 2010.

[33] S. Jang and G. A. Voth, "Path integral centroid variables and the formulation of their exact real time dynamics," *The Journal of Chemical Physics*, vol. 111, no. 6, pp. 2357–2370, 1999.

[34] M. Ceriotti, M. Parrinello, T. E. Markland, and D. E. Manolopoulos, "Efficient stochastic thermostatting of path integral molecular dynamics," *The Journal of Chemical Physics*, vol. 133, no. 12, p. 124104, 2010.

[35] R. Kubo, "The fluctuation-dissipation theorem," *Reports on Progress in Physics*, vol. 29, no. 1, p. 255, 1966.

[36] D. Marx, M. E. Tuckerman, and G. J. Martyna, "Quantum dynamics via adiabatic ab initio centroid molecular dynamics," *Computer Physics Communications*, vol. 118, no. 2-3, pp. 166–184, 1999.

[37] D. Quigley and M. I. J. Probert, "Langevin dynamics in constant pressure extended systems," *The Journal of Chemical Physics*, vol. 120, no. 24, pp. 11432–11441, 2004.

[38] J. Cao and G. A. Voth, "The formulation of quantum statistical mechanics based on the feynman path centroid density. ii. dynamical properties," *The Journal of Chemical Physics*, vol. 100, no. 7, pp. 5106–5117, 1994.

[39] I. R. Craig and D. E. Manolopoulos, "Inelastic neutron scattering from liquid para-hydrogen by ring polymer molecular dynamics," *Chemical Physics*, vol. 322, no. 12, pp. 236 – 246, 2006.

[40] S. J. Clark, M. D. Segall, C. J. Pickard, P. J. Hasnip, M. I. J. Probert, K. Refson, and M. C. Payne, "First principles methods using castep," *Zeitschrift für Kristallographie - Crystalline Materials*, vol. 220, pp. 567–570, 2013/07/01 2005.

[41] I. R. Craig and D. E. Manolopoulos, "Quantum statistics and classical mechanics: Real time correlation functions from ring polymer molecular dynamics," *The Journal of chemical physics*, vol. 121, p. 3368, 2004.

[42] M. Ceriotti, G. Bussi, and M. Parrinello, "Colored-noise thermostats à la carte," *Journal of Chemical Theory and Computation*, vol. 6, no. 4, pp. 1170–1180, 2010.

[43] R. H. Bartels and G. W. Stewart, "Solution of the matrix equation ax + xb = c," *Commun. ACM*, vol. 15, pp. 820–826, Sept. 1972.